PROPOSAL : MAGIC option

Towards a Conceptual Design of the NEXT-100 detector based on a Micromegas charge readout

O. Ballester[1], J. M. Carmona[2], J. Castel[2], S. Cebrián[2], T. Dafni[2], E. Ferrer-Ribas[3], I. Giomataris[3], H. Gómez[2], D. C. Herrera[2], F. J. Iguaz[3], J. Illa[1], I. G. Irastorza[2,*],G. Jover-Manas[1], G. Luzón[2], T. Lux[1], C. Martin[1], J. Rico[1,4], A. Rodríguez[2], F. Sánchez[1], L. Seguí[2], A. Tomás[2], J. A. Villar[2]

[1]Institut de Física d´Altes Energies (IFAE), Edifici Cn, Universitat Autònoma de Barcelona, 08193 Bellaterra (Barcelona), Spain
[2]Laboratorio de Física Nuclear y Astropartículas, Universidad de Zaragoza, 50009 Zaragoza, Spain
[3]IRFU, Centre d'Études Nucléaires de Saclay (CEA-Saclay), 91191 Gif-sur-Yvette, France
[4]Institució Catalana de Recerca i Estudis Avançats (ICREA), 08010 Barcelona, Spain

[*]contactperson

Contents

1 Introduction: Goal of this document

This document is a proposal for a CDR (Conceptual Design Report) of the NEXT-100 detector with a MAGIC readout technology choice. The baseline of this proposal is to read the ionization signals on the NEXT TPC with a charge gain readout based on pixelized Micromesh Gas Structures (Micromegas), from which both the energy and topological information of the event is extracted. Full fiducialization (via t_0 measurement) is obtained by the measurement of the primary scintillation by means of a sparse photomultiplier tube (PMT) array behind the TPC cathode (see figure 1).

The goal of the document is to gather all the relevant information available at present regarding this technological option, its proposed realization, its merits and expected performance and its risks, in order to facilitate the decision-making process within NEXT. Information on detector subsystems common to alternative readout technological options (e. g. shielding, vessel, gas system, etc...), will not be covered in the present document, except in the specific aspects to which the proposed readout choice would affect.

Beyond the description of this detector baseline, we also express our view on the course of action that we propose for the collaboration, regarding the realization of intermediate detectors and the attitude towards possible detector enhancements that may become viable in the near future. We propose a staging scenario which includes a demonstrative intermediate detector (NEXT-10) before the full-size NEXT-100 detector, in close connection with R&D activities in the collaboration (in particular the ones carried out with the NEXT-1 setups). Starting with the baseline design here described, the workplan of the collaboration could eventually include stages (already for the first version of NEXT-100 or as second enhanced version of the detector) incorporating one or more improved modifications of the baseline that could have become established in the meantime. We anticipate in this document a series of such possible improvements that, with the information available at the moment, we consider of high potential.

The document is structured as follows. We start with an introductory discussion on NEXT and the technology decision in section 2, to follow with the presentation of the basis of the Micromegas technology choice in section 3, and its specific implementation proposed in 4. In section 5 we discuss the sources of background, the shielding and the radiopurity data on which we develop the background model in section 6. In that section we also present the expected performance of the detector in terms of sensitivity to the $0\nu\beta\beta$ signal. In section 7 we anticipate some operation and maintenance issues and in 8 some costing information. In section 9 we identify some risks and propose corresponding mitigation plans. In section 10, we present some possible improvements that could be incorporated in future stages of the baseline design with enhanced sensitivity. We finish this document with a proposed course of action for the collaboration in section 11 and the overall summary in section 12. We leave for several appendixes a series of more detailed information on issues that are referred to throughout the document.

2 NEXT: a high pressure Xe TPC

NEXT intends to search for the $0\nu\beta\beta$ decay of ^{136}Xe using a gaseous Xe Time Projection Chamber (TPC). The main point motivating this approach with respect to most competing $\beta\beta$ detection techniques is that a gas TPC has access to the topological information of the event (the two electron tracks) opening the way to signal identification, and enhanced background rejection. Moreover, and thanks to modern concepts in TPC readouts, this extra handle comes while maintaining a good energy resolution, despite other tracking $\beta\beta$ detection approaches, including previous TPC implementations. As discussed later on in section 6, the background level and the energy resolution are the two most important parameters leading the figure of merit of a $0\nu\beta\beta$ experiment.

The choice of technology for the NEXT readout, and by extension of every component of the detector must be done paying attention to the ability to exploit both mentioned aspects: event topology information and good energy resolution. The energy resolution is directly determined by the nature of the signal detection in the readout. Besides, the readout has also an impact on the background of the detector, both through the radioactivity of the readout components or via the quality of the topological information it provides. Ideally, when comparing the merits of different options, one should quantify the impact that such an option has in the final overall figure of merit through both energy resolution and background. This is done in section 6 for the option here proposed, to the extent the currently available information allows us.

Other more practical aspects, although difficult to quantify, are of importance and need to be considered too. NEXT has an ambitious schedule, bound by the timeliness of a result with a 100 kg prototype, NEXT-100, current horizon of the collaboration. To underestimate the risks of the technological choice could lead to unacceptable delays in the NEXT schedule, therefore under certain conditions conservativeness can be a bonus. Another aspect is the possibility of accommodating future improvements that could come in ongoing R&D activities. These R&D could provide important sensitivity enhancements or be the key for eventual risk mitigation. The adoption of a flexible enough option capable of incorporating these enhancements when available is also a bonus. Last but not least, the cost is another important factor to be considered.

In the following sections we expose a baseline concept for the NEXT detector based on a Micromegas charge readout. We believe this option represents at the moment the best compromise fulfilling the above considerations regarding expected performance in background and energy resolution, plus conservativeness, flexibility to future enhancements and cost. We will try to argue these reasons in subsequent sections.

3 NEXT readout: technological baseline

The main element of this proposal is a *microbulk* Micromegas readout placed at the TPC anode. The Micromegas is one of the most successful developments among the so-called micropattern gas detectors (MPGD), the modern version of the multiwire proportional counter (MWPC) charge readouts, but using instead microstructures engraved on plastic substrates, much like printed circuits. MPGDs are overriding conventional MWPCs in flexibility and performance, and are object of very active study and development since more than 20 years[1]. Micromegas stands out among MPGDs in aspects like energy resolution, stability of operation or radiopurity, among others, and are recently attracting much attention for rare event applications [1, 2, 3, 4, 5, 6].

The Micromegas devices are characterized by a micromesh suspended over the pixelized anode plane by some insulator pillars (or supporting structure), forming a thin gap (of about 25 – 150 μm) where the charge amplification takes place. The primary charge reaches the mesh after drifting through the conversion volume, enter the gap and triggers the avalanche which induces detectable signals both in the anode and in the mesh. While the anode is usually patterned (e.g. pixelized) and therefore provides topological information on the primary charge cloud, the mesh is common to all or several pixels, and therefore provides a redundant reading of the same avalanches with the possibility of integrating the charge over a wider area.

Of the several manufacturing techniques available to fabricate Micromegas readouts, we focus on the *microbulk* Micromegas [7]. This technique, jointly developed by CEA and CERN, allows to pro-

[1] RD-51 collaboration

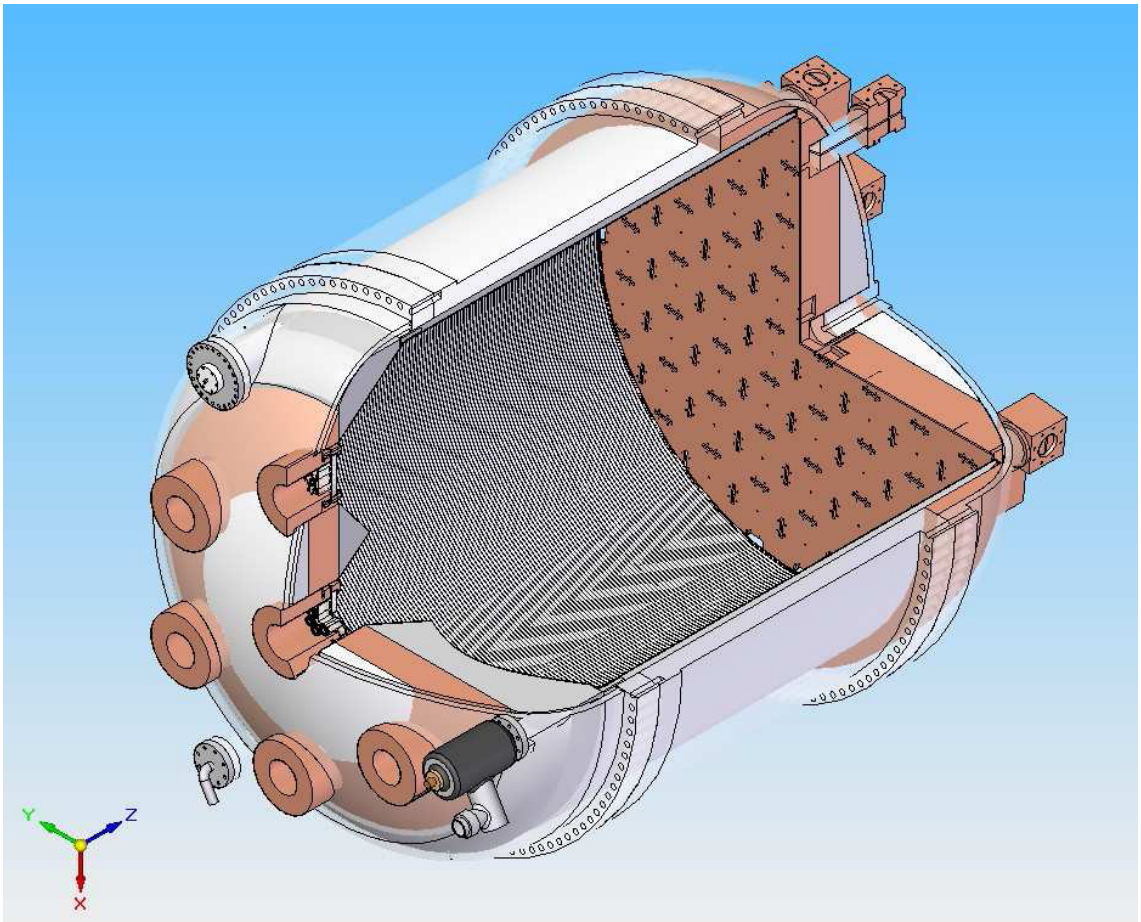

Figure 1: General design of the NEXT-100 detector with the baseline configuration proposed in this document. At the front the cathode side of the TPC can be seen with the outlets lodging the PMTs for t_0 measurement. At the back the anode side, with the modular structure supporting the microbulk Micromegas charge readout for energy and topology measurement.

vide all-in-one readouts out of double-clad kapton foils. The mesh is etched out of one of the copper layers of the foil, and the Micromegas gap is created by removing part of the kapton by means of appropriate chemical baths and photolithographic techniques. The fabrication technique has been developed substantially during the last years and the resulting readouts have very appealing features, outperforming previous generations of Micromegas in several aspects. The mechanical homogeneity of the gap and mesh geometry is superior, and in fact these Micromegas have achieved the best energy resolutions among MPGDs.

The use of microbulk readouts in high pressure pure Xe has been considered and proposed already at the conception of NEXT. Since then, a substantial body of experimental data have been generated by NEXT groups (some of it already published recently [8, 9, 10, 11]) which demonstrate that application of microbulks in NEXT is feasible. While the overall body of data is presented in some detail in appendix A for reference, we can conclude that:

1. Microbulk readouts can operate at high pressure pure Xenon (tested up to 10 bar) and they do

amplify with gains above 100. This is a remarkable result which compares very positively with other MPGDs. Operation of charge gain devices in pure noble gases is problematic due to the rapid photon-driven expansion of the avalanche, which makes the detector quickly depart from the proportional amplification regime into the Geiger regime (this being the reason of the use of gas quenchers in usual gas TPCs). We speculated that the confinement of the avalanche in microbulk readouts (inside the kapton cell formed below each micromesh hole) prevents the photons from expanding the avalanche far away, and acts as a sort of quencher. Although more studies are ongoing to test this hypothesis, this seems to be now corroborated experimentally by the relatively high gains indeed measured with microbulks.

2. Energy resolutions have been measured with both low energy photon (22 keV and 60 keV) and high energy alphas (5.5 MeV). In overall, the results are compatible with energy resolutions of 1% FWHM at the $Q_{\beta\beta}$ at 2 bar pure Xenon, with indication of continuous widening of the resolution for higher pressures, having 2% and 3%, for 5 and 10 bar respectively (we refer to appendix A for details on these data). Although plans to improve these results are underway, we consider the previous numbers as realistically achievable in NEXT. We will develop the rest of the document with those numbers as reference values for the energy resolution.

3. Microbulk readouts are very radiopure objects. Various samples of the raw materials as well as of processed readouts have been measured [11] with a high purity Ge detector, yielding values on the minimum detectable level of the measurement, and corresponding to less than 30 μBq/cm^2 for Th and U chains and about 60 μBq/cm^2 for ^{40}K. These values constitute an upper limit imposed by the small mass of the measured samples, and certainly they have even lower levels of contamination, as suggested by the amount and type of raw materials (kapton and copper). Moreover, taking into account that the studied readouts were manufactured without any specific control of the radiopurity, it should be possible to improve them in case traces of radioactivity is found in future more sensitive measurements.

These results are the technological baseline of this proposal, the practical realization of which is developed in the next sections.

4 Proposed realization

4.1 Topology/energy readout: Micromegas

The proposed realization of the Micromegas readout is based on a mosaic structure of identical, relatively small, modules. Each of these modules is a single microbulk readout of 16×16 cm^2 of active area and patterned with an array of 1 cm^2 pixels, as shown in figure 2. This module is of similar dimensions and number of channels as the microbulk readouts already manufactured for the NEXT prototypes (both NEXT-0-MM and NEXT-1-MM, see appendixes) allowing us to minimize the risks derived from possible new manufacturing challenges or unknowns. The Unizar group is already working with CERN within the RD-51 collaboration to enlarge the maximum dimensions[2] of single microbulks to 30 cm of side. If successful this would further simplify the design here proposed. All pixels are extracted independently by strips engraved in the same kapton foil of the Micromegas, going towards contacts placed a few cm away as shown in figure 2. The mesh of each module is segmented into 4 parts (of 8×8 cm^2 area each),

[2]The limitation coming from the fabrication equipment available

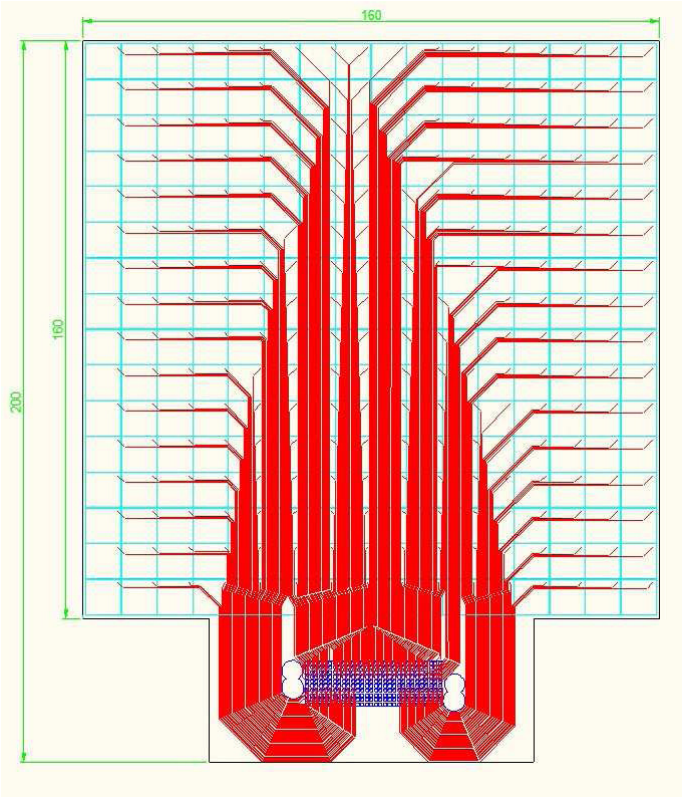

Figure 2: Design of the single module microbulk readout of an active area of 16×16 cm^2. Each pixel is indicated in light blue, and the strips connecting each of the pixels to the contact connector pad array in red. The connector is placed in the flap at the lower side of the figure.

each of them read out independently. If deemed necessary (see discussion of section 6) a finer mesh segmentation can be considered.

The microbulk are light, flexible structures composed of kapton and copper. In order to rigidify the readout, they will be glued into thick metallic supports made of high purity copper, providing also a good protection against electronic pick-up noise. The support will be machined in order to allow the assembly of the modules and proper extraction of the signals. The concept is sketched in figure 3. The signals are brought by strips into a contact connector (of the kind already tested in NEXT-1-MM) in the very microbulk plane, placed few cm away from the active zone in a flexible flap that is folded down as shown in figure 3 through a hole in the metallic support. This allows an elegant, light-weight, solderless, radiopure extraction of the signals, allowing a proper staging of neighboring modules to compose the mosaic readout. The extraction of the signals out of the vessel is therefore achieved by means of one 300 channel flat cable and a 300-channel feedthrough per module of the types already developed for NEXT-1-MM.

The tolerances achievable in the assembly of neighboring modules can be well below the mm. However, no dead zone is allowed in the readout if we want to keep high energy resolution. This is achieved by means of the "rim" concept. Around the mesh of each microbulk an independent strip of about 100-200 μm is engraved (in the same process of the mesh manufacturing), and at operation time it is powered independently at a few volts above the mesh voltage. The drift lines near this structure are slightly bent, like shown in figure 4. As a consequence, the electrons that would otherwise drift towards a region dangerously close to the edge of the microbulk (potentially dead zone), are gently pushed inwards to the center of the last pixel of the active zone. In this way absolutely no charge is lost. The overall deformation of the drift lines is much less than the pixel size, so there is no consequence on the topology

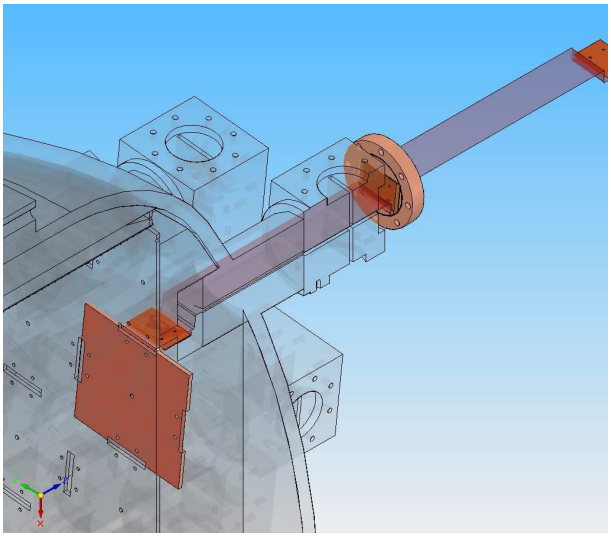

Figure 3: Sketch of the single module mechanics. Highlighted are the microbulk copper support, the feedthrough and the flat cable connecting at the flap of the microbulk and bringing the signals to the feedthrough.

information.

In total, about ∼50 modules of the ones described are needed to cover a circular area of 1.3 m diameter, amounting to a total of ∼13500 pixels. The material radiopurity budget is kept to a minimum: mostly high purity copper, kapton in the Micromegas and the flat cables, polyamide PCBs in the head of the flat cables and the feedthroughs, a small amount of epoxy to glue the Micromegas, and the small sandwich pieces of the contact connectors, made of LCP (liquid crystal polymer). The contribution to the background from these materials is discussed in section 6.

4.2 Measurement of t_0

The proposed readout for the primary scintillation is a set of PMTs placed behind the TPC cathode. The combined requirement on radiopurity and pressure makes the selection of a commercial PMT for NEXT difficult. However, the requirement for t_0 measurement is just that sufficient light is detected to have a robust t_0 signal. For this a relatively small number of PMTs is needed, and therefore a solution based on placing the detectors outside the vessel, facing quartz windows seems plausible, skipping the need for an R&D to reinforce the PMTs, and allowing to choose existing very radiopure PMTs, like the Hamamatsu R8520. Other options could also be envisaged, like the larger, also radiopure, R10789 developed by the XMASS collaboration, if they become available in the meantime.

The realization of this PMT array in our proposal is as follows. The endcap of the high pressure vessel will be furnished with 7 cylindrical outlets of the same high purity copper (joint to the body of the endcap by means of electron beam welding) and 10 cm inner diameter. These outlets differ from standard CF-100 nipples in that they prolong inwards and they are equipped by a flange in the inner side of the cylinder instead of the outside. This flange is used to install a 2 cm thick quartz window, which closes tightly and supports the 10 bar pressure. A number of PMTs (7 of the R8520 model) are thus placed in the inside of each of these cylinders, under one atmosphere, optically coupled to the window, as shown in figure 5. Preliminary simulations show that this arrangement of 49 PMTs are enough to provide a robust t_0 signal. The windows must be of a material transparent to the Xe wavelength (like Suprasil quartz) or be equipped with wavelength shifter coating, like TPB. Optionally, the cylinder can also be tightly closed in the outside, in case it is considered convenient as a safety measure against loss of Xe by cracking/leaking through the window flange.

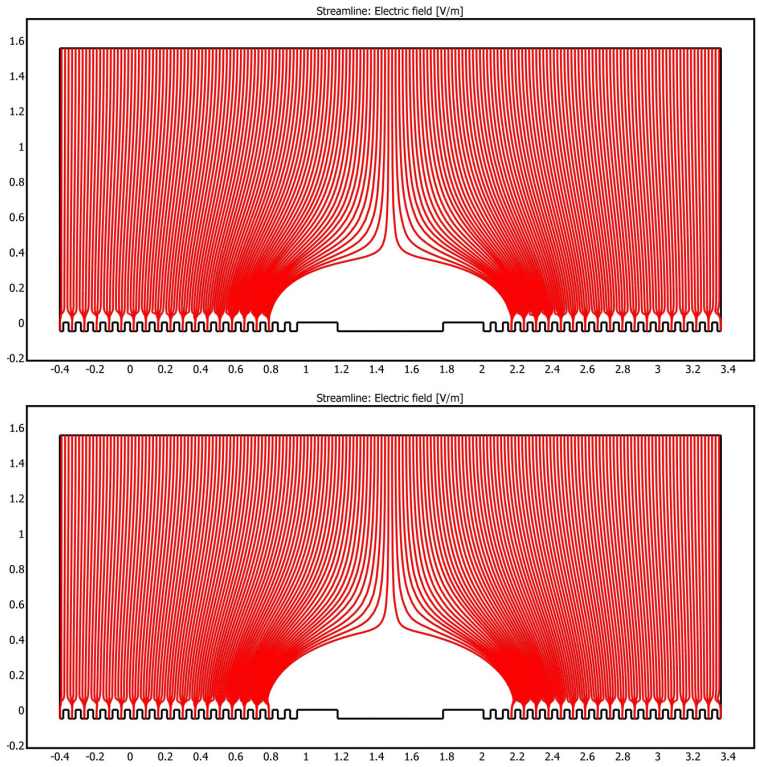

Figure 4: Simulation (2D-approximation) of the rim effect on the drift lines around the boundary between microbulk modules. Dimensions are expressed in mm. The rim is 200 μm metallic strip in both the microbulk edges and are at 200 μm distance from the Micromegas active area. They are placed at -255 V while the mesh is at -250 V (i.e. 5 V of difference) above, the Micromegas anode is grounded and the drift field is 100 V cm^{-1}. The plot at the bottom is the same but with the rim at -260 V. In both cases all drift lines that otherwise would have fallen on the dead area are gently pushed into the active area of the Micromegas, the overall distortion being below the mm scale.

This scheme has important advantages. It is conservative, as no R&D is needed to reinforce the PMTs. It is mechanically simple, as the quartz window is placed from the inside and the pressure works positively towards tightening up the flange. It is a moderately radiopure option, allowing us to use the most radiopure PMT commercially available. We have to stress, however, that the 49 PMTs placed in this way constitute still an important contribution to the radioactive background of this proposal as studied later in section 6. Although we keep this PMT arrangement as our choice for t_0 measurement in this baseline configuration, we consider that alternative options avoiding PMTs completely are possible and very motivated. These options will be discussed in section 10.

4.3 Vessel and field cage

The Micromegas charge readout and the PMT readout described in the previous subsections being the two main ingredients of this baseline design, we describe in the following the remaining inner elements of the configuration proposed. This has been defined following criteria of radiopurity, conservativeness, current experience and compatibility with the previous readout elements. However, other solutions may

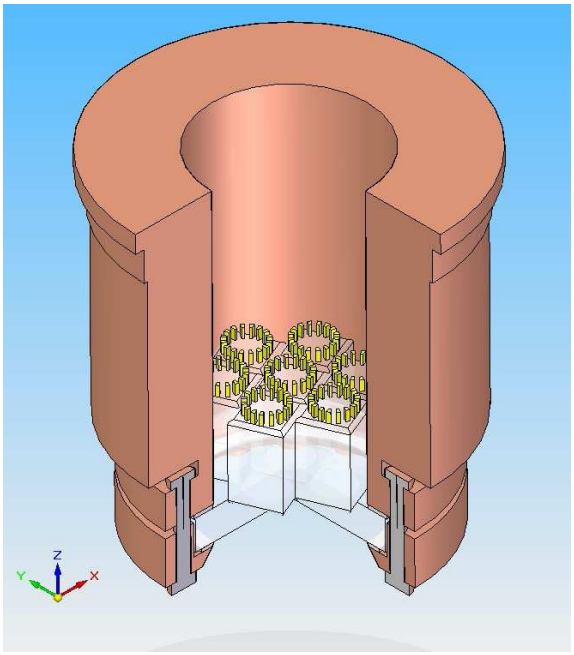

Figure 5: One of the copper cylinder welded to the cathode endcap, lodging seven PMTs facing a quartz window.

eventually appear more convenient in the light of future work of the *vessel working group*. For the purpose of sensitivity estimation of our baseline design, we have defined the detector materials as follows.

We propose to build the vessel out of high purity oxygen-free copper (C10100). Apart from being the metallic material for which the lowest concentrations of radioactive contaminants are routinely achieved, it represents a safe choice as it systematically shows good radiopurity levels rather independently of the provider. The relatively poor mechanical properties of copper are overcome by allowing for relatively thick walls in the design (up to 3 cm thanks to reinforcements). The amount of material used in the vessel plays also the role of the innermost part of the shielding, so in a shielding configuration based in a lead+copper castle, this choice is natural as it subtracts from the inner copper lining required for shielding, as discussed in the next section.

The vessel is depicted in figure 1. It is composed by 3 parts: one cylindrical piece with an inner diameter of 1350 mm and a total length of 1216 mm and 2 torispherical endcaps. All welding is performed by electron beam welding (EBW), with no addition of material in the welding and preserving the radiopurity of the copper. In order to ensure a reliable flange sealing PTFE (teflon) gaskets and C10100 copper bolts are used. The inside of the endcaps is partly filled with extra copper and PTFE pieces for electrical protections, to avoid empty space that would otherwise be filled with Xe, and to effectively use this space as inner shielding. The remaining empty space, mostly between the cathode and the PMTs represents 20% of the total volume. This space is necessary to keep a safe distance between the cathode at HV and the grounded PMTs/flanges, avoiding spurious electroluminiscence signals.

The drift region is of cylindrical shape and has a diameter of 131 cm and a drift distance of 131 cm. It is delimited by the field cage, the micromegas readout and the cathode composed by wires or a very transparent grid. The field cage consist of 2 mm wide copper strips imprinted on a Teflon substrate of cylindrical shape. The distance between strips is 1 cm and they are interconnected by SMD5 resistors using silver soldering. The thickness of the Teflon substrate is 2 cm. The breakdown voltage of Daikin PFA Teflon is 28 kV/mm, (tested for thicknesses of $\sim$1 mm, but this value depends strongly on the thickness of the sample), so although 2 cm should be sufficient for holding voltages at the cathode of

130 kV (corresponding to a drift field of 1 kV/cm), specific tests are needed at the real voltages and dimensions.

The sensitive volume dimensions being fixed (partly for historical reasons) to hold 100 kg of Xe at 10 bar, the current geometry will hold only 80 kg at 8 bar, due to the 20% extra volume outside the field cage. Instead of rescaling the dimensions to go back to 10 bar we decided to keep the stated dimensions, and therefore an operation pressure of 8 bar for our baseline option, without particular optimization, with the aim of: 1) providing a safety margin in the operation of Micromegas readout at high pressure and in the achievable energy resolution (see discussion in section 6 and 2) adding a factor of conservativeness in our studies on topology cuts, which efficiency and rejection factor have been studied for a Xe density corresponding to 10 bar.

Finally, the front-end electronics associated to the Micromegas readouts are placed at the outer side of the anode endcap, at a position as close as possible to the readouts as allowed by the condition that their radioactivity's contribution to the background be negligible. For that they are immersed in the shielding, and attenuated by all the copper pieces allocated in the endcap and, possibly, part of the inner shielding, depending on the radioactivity of the final electronics. The length of the flat cables will therefore be around 50 cm, not very different to the distance currently used in NEXT-1-MM. While electronics based on the AFTER chip (T2K TPC electronics) is being used for the test with NEXT-1-MM (see appendix A and B) it is still to be determined if the same hardware is adequate for NEXT-100. In any case, it should follow a similar philosophy.

5 Radiopurity and shielding

Backgrounds in rare event experiments may come from external radiation (e.g. from radioactivity of the laboratory rocks or airborne radon) or from radioactivity of the components of the detector setup itself. The first category is dealt with by appropriately shielding the detector and the second by controlling the radiopurity of every detector component, assuring that sufficiently radio-clean materials are used. In the following paragraphs we introduce the basic elements and assumptions on shielding and radiopurity, on which we later build up the background model to estimate the performance of the option proposed. Although a more detailed sensitivity calculation is performed later, let us stress that for NEXT to be sensitive to a signal of a few counts per year (corresponding to the $0\nu\beta\beta$ for $m_{\beta\beta} \sim 50 - 100$ meV) the background at $Q_{\beta\beta}$ must be below a few $\times 10^{-4}$ counts keV^{-1} kg^{-1} y^{-1}. This strong requirement will drive the following discussions.

5.1 Shielding

The main monoenergetic gamma line above $Q_{\beta\beta}$ in the natural radioactivity is the 2.615 MeV photons coming from the ^{208}Tl isotope of the ^{232}Th radioactive chain with a flux around 0.13 γ/cm^2/s (according to measurements performed at LSC [12]). The photons of 2.448 MeV coming from ^{214}Bi of the ^{238}U chain, being much less abundant, could be more dangerous since they are only 0.4% away from the $Q_{\beta\beta}$ energy, unresolved from our signal peak even with the best energy resolutions achievable by NEXT. Simulations show that typically their contribution is similar to that of the 2.615 MeV photons for similar original impurities of ^{208}Tl and ^{214}Bi. Moreover, since both energies are quite close, attenuation studies for 2.615 MeV photons are roughly valid for 2.448 MeV photons too.

Preliminary studies performed by the NEXT *shielding working group* indicate that the thickness of the shielding needed to attenuate the external radiation down to negligible levels for NEXT should be around 25 cm in the case of lead and almost 3 m in the case of water. We could always go for a mixed

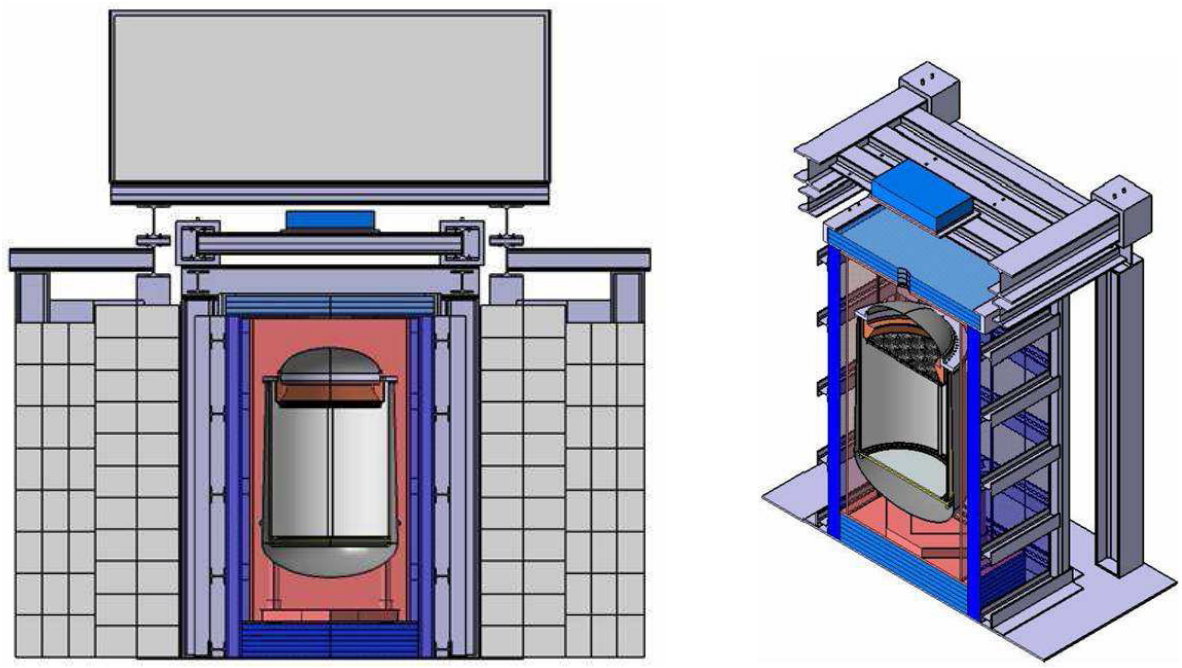

Figure 6: Possible realization of the lead+copper version of the NEXT shielding among the ones considered by the NEXT shieling group (designed by the Ciemat group). In this design the outer 10 cm of lead is replaced by 1 m of water, equivalent in attenuation power. We refer to [13] for more details.

option in which 1 cm of lead would be substituted for 10 cm of water (or other material with a density close to 1 g/cm^3, e.g. polyethylene). Moreover, the innermost part of the shielding must comply with strong radiopurity conditions (like the other detector components), as the contribution of its radioactivity should not exceed the radiation being shielded by it. This seems to be achievable both by a design based on a water tank or a design based on lead and copper castle, solutions studied in the *NEXT shielding report*. For the sake of concreteness, we focus in the second of such options, a shielding based on a lead wall with an inside lining of high purity copper. In fact, the material of this lining is exactly the same copper as the one of the detector vessel. From the point of view of its shielding effect and radioactivity emissions, both media are identified. Due to self-shielding, only the 3 innermost cm of shielding/vessel have a relevant contribution to our background model. A possible realization of such option is depicted in figure 6.

Another source of background, deserving special attention, is radon and its progeny. As part of the ^{238}U natural chain, ^{222}Rn gas can escape out of materials and diffuse through others with a rather complex dynamics during its lifetime ($T_{1/2}$=3.8 days). Its progeny can deposit on surfaces, especially those electrostatically charged. Among the progeny we have ^{214}Bi, a dangerous source of background for NEXT, as mentioned before.

Airborne ^{222}Rn in the atmosphere of underground laboratories can be rather high and variable due to emanation from the rock walls, with typical values around $\sim$100 Bq/m^3 (although it can be substantially lowered by a good quality forced ventilation). If this concentration is assumed also for the empty spaces inside the shielding this would constitute an unacceptable source of background for NEXT. Therefore, the first measure is to enclose the shielding in a radon-tight tent, under a clean (e.g. N_2) atmosphere, capable of bringing down the ^{222}Rn concentration inside the shielding to levels of $\sim$10 mBq/m^3, i.e.

4 orders of magnitude below the external concentration (conservative estimation assuming a rather large internal empty volume of 2.5 m^3, for example due to a 20 cm gap between vessel and shielding).

Despite a good isolation with the external ^{222}Rn, materials inside the shielding will still emanate radon at a rate which depends on the ^{238}U contamination of the material and its radon diffusion coefficient (which one needs to measure experimentally). A continuous flush of radon-free gas, purging all empty space inside the shielding at a sufficient rate, is a necessary element against emanation by the materials inside the shielding and outside the vessel.

Approximate but conservative estimations can be done for the amount of ^{222}Rn emanated by the lead and copper of the shielding and the outside of the vessel. Assuming 10 μBq/kg for ^{238}U contamination in copper and 1 mBq/kg in lead and a radon diffusion distance of 0.1 mm in both lead and copper, we obtain a total emanation rate of around 2 Bq. This value implies a contribution of a few 10^{-4} counts keV^{-1} kg^{-1} y^{-1}at $Q_{\beta\beta}$. To reduce it by one order of magnitude the whole volume must be renewed every 13.4 hours while two orders implies a renewal every 1.3 hours. Conservatively using 2.5 m^3 as the total empty volume inside the shielding (5 l of liquid N_2 are enough to fill up this volume), flushing rates above $\sim$ 10 lN_2/day should be sufficient to bring radon levels below NEXT sensitivity, assuming the flushing is performed effectively over all inside volume, and no dead spaces are left for radon to grow up. Emanation inside the vessel into the Xe itself must also be carefully studied because no flushing is possible there. Although the alphas from ^{222}Rn in the sensitive volume could give a precise information of the amount of ^{222}Rn being emanated at a particular moment into the detector gas, they do not help in tagging the background events induced by the ^{214}Bi deposited in the cathode. A preliminary calculation of the inwards emanation of the materials considered in our baseline design has been done conservatively assuming that all emanated ^{222}Rn ends up as ^{214}Bi surface contamination in the cathode. Thanks to the extraordinary radiopurity requirements (see later) of the inner materials, and especially the copper vessel, the contribution of this effect seems to be negligible. In any case, care must be taken also with the materials in contact with the Xe all along the gas system (tubes, valves, filters, etc...) as they all can potentially emanate radon which, due to the recirculation, will end up in the detector vessel. The case of ^{220}Rn from the ^{232}Th chain has not been considered since it decays in less than 1 min into polonium which it is not a gaseous isotope and the emanation is expected to be much lower.

Of special relevance is the Radon concentration in water for the case of the water shielding (GERDA gives data for radon contamination around 7-19 mBq/m^3). The shielding design in this case should also foresee a radon filtering stage for the water system.

Therefore, the overall radon dynamics can be rather complex, and the problem of controlling its concentration close to the sensitive volume below the required levels for state-of-the-art competitive low background experiments is always a challenging one. This is an essential point for NEXT, beyond the readout technological decision which is the purpose of this document. As a working hypothesis for the present document, we assume that the shielding for the experiment will succeed in bringing the effective radon concentration in the inside of the shielding to levels below $\sim$10 mBq/m^3, with negligible contributions to the background. Therefore, we will not include a contribution from Radon in our background model later on in section 6.

Other possible external sources of background are neutrons, whether produced by natural radioactivity in the walls or shielding or as secondary products of cosmic muons. Preliminary estimations seem to point that these contributions are very much below the level of concern for NEXT. High energy gammas can be produced in muon-induced electromagnetic cascades. Although they too seem to be of no importance for NEXT, they could be partially tagged by using active muon veto in the shielding.

To summarize, for the purpose of the present document we assume that the shielding fulfils the following specifications, which allow us to neglect in our background model all external gamma contri-

butions, all radioactive emission from shielding materials (other that the innermost 3 cm of copper) and contribution from radon and its progeny:

1. The shielding should be thick enough to attenuate external photons down to levels corresponding to background levels in NEXT below $\sim 10^{-4}$ counts keV^{-1} kg^{-1} y^{-1}. This thickness corresponds to 25 cm of lead.

2. The radiopurity of the different layers of the shielding must be such that each of the layer's contribution to the background, after attenuation of the material inside that layer, does not amount in total to more than the stated $\sim 10^{-4}$ counts keV^{-1} kg^{-1} y^{-1}. The radiopurity of the innermost layer, in particular, has the strongest radiopurity constraint, at the level of the detector components themselves. This is achieved by the lead castle option by using an inner lining of about ~ 5 cm high purity copper ($\sim 10\,\mu$Bq/kg)

3. The shielding is built with anti-radon measures mentioned above (radon-tight tent, radon-free gas flushing system), so that it efficiently fights against radon emanation from materials or radon diffusion from the laboratory air, and bring the radon concentration down to negligible levels for NEXT.

This assumptions justify the exclusion from our background model of all external sources of background as well as radioactivity from the shielding materials, other than the innermost 3 cm of copper of the shielding or vessel. We will focus in the following in the identification of all possible internal sources of background and therefore on the radiopurity of the inner materials.

5.2 Radiopurity

Despite the advantage offered by a gas TPC using the event topology to reject backgrounds, still the strictest requirements on radiopurity are to be applied to the materials composing the inner part of the detector. Eventually, all materials entering the design must be screened either by direct gamma counting with germanium detectors or by alternative methods like Mass Spectrometry (GDMS and ICPMS) or Neutron Activation Analysis (NAA). The requirement on a particular component or, conversely, the criteria to use or not a given material for such component must consider its radiopurity, the mass of such material in our geometry and the particular position with respect to the sensitive volume of the detector. All these elements are inputs of the background model that, based on Geant4 simulations, quantifies the contribution of each element to the final experimental background. This model, described in detail in section 6, has been used to define the detector configuration sketched in the previous section, and to select the best materials minimizing the background.

For the purpose of this CDR, we have conservatively relied on materials and components with levels of radioactivity known in the community of low background techniques, measured in the context of several rare event experiments. We refer to the *NEXT radiopurity group report* for further details on sources and methods [23]. For some cases, data from measurements performed by the Unizar group are available. Table 1 summarizes the materials finally retained as relevant for the baseline design here proposed, their measured activities of ^{238}U,^{232}Th and ^{40}K (although this last isotope will not contribute to NEXT background), the method of measurement and the source reference. All entries entering the background model of section 6 are listed in this table. Additional entries considered interesting are also included, like additional measurements of the same material by other methods or other groups, or measurements of materials or components that could be used as alternative choices. The measurements number 2, 5,

#	Material	Method	Unit	^{238}U	^{232}Th	^{40}K
Metals						
1	Lead Cometa	GDMS	mBq/kg	<0.372	<0.073	<0.31
2	Copper Luvata C10100	Ge spectroscopy	mBq/kg	<11.0*	<9.7*	<17.7*
3	Copper Luvata C10100 hot rolled	GDMS	mBq/kg	<0.012	<0.004	0.060
4	Copper Luvata C10100 cold rolled	GDMS	mBq/kg	<0.012	<0.004	0.090
5	Stainless Steel Pfeiffer 304-L	Ge spectroscopy	mBq/kg	14.8±2.8	10.4±2.0	<16.6*
Detectors						
6	Micromegas without mesh [11]	Ge spectroscopy	mBq/cm^2	<0.040	0.005±0.002	<0.046
7	Microbulk-Micromegas [11]	Ge spectroscopy	mBq/cm^2	0.026±0.014	<0.009	0.057±0.025
8	Kapton-copper foil [11]	Ge spectroscopy	mBq/cm^2	<0.011	<0.005*	<0.008*
9	Copper-Kapton-copper foil [11]	Ge spectroscopy	mBq/cm^2	<0.011	<0.005*	<0.008*
Plastics						
10	Kapton film [14]	ICPMS	mBq/kg	12±4	0.6±0.2	9±2
11	Kapton [15]	NAA	mBq/kg	<99.2	<36.5	58.9±3.1
12	TEFLON DuPont NXT75 M111 [16]	NAA	mBq/kg	<0.023	<0.006	0.099±0.040
13	TEFLON [17]	Ge spectroscopy	mBq/kg	<24.8	<16.2	<341
14	VITON Johannsen AG [16]	Ge spectroscopy	mBq/kg	868±87	130	2170±226
15	PEEK	Ge spectroscopy	mBq/kg	36.3±4.3	11.6±2.2	8.3±3.0
16	VECTRAN(Liquid Crystal Polymer)[18]	ICPMS	mBq/kg	<1.24	<0.12	1395
17	Two component epoxy, Resin 20-3001R clear, catalyst 20-3001C, 1:1 mix [16]	NAA	mBq/kg	<0.55	< 0.094	< 0.62
Connectors, cables,...						
18	TIG Welded [16]	ICPMS	μBq/cm	<0.126±0.042	<0.040	—
19	INDIUM New Brunswick Plating 190 [16]	ICPMS	mBq/kg	0.23±0.03	0.030±0.005	5.86±0.68
20	SILVER soldering [15]	GDMS	mBq/kg	<0.12	<0.29	<0.40
21	WIRES MacMaster-Carr 7512 K552 2nd shipment [16]	ICPMS	mBq/kg	0.198±0.012	0.117±0.008	<1.9
22	WIRES Atlas Axon [14]	Ge spectroscopy	mBq/kg	<12	<12	230±60
23	Circuit Board Cuflon Edelweiss [19]	Ge spectroscopy	mBq/kg	<23	<30	400±200
24	Surface mount precision plate, SM5D, 700MΩ resistors [20]	Ge spectroscopy	mBq/pc	0.027±0.003	0.014±0.003	0.19±0.03
PMTs, windows						
25	PMT R10789 [21]	Ge spectroscopy	mBq/PMT	0.70±0.28	1.51±0.31	<5.1
26	PMT R8520 [22]	Ge spectroscopy	mBq/PMT	0.25±0.04	0.21±0.05	9.3±1.1
27	Heraeus 2 quartz [16]	NAA	mBq/kg	0.068±0.027	0.027±0.005	0.062±0.016
28	Heraeus Suprasil Quartz [16]	NAA	mBq/kg	0.26±0.11	0.240±0.057	—

Table 1: Summary of measured activities of ^{238}U , ^{232}Th and ^{40}K in different materials. * Level obtained from the minimum detectable activity of the detector (MDA).

6, 7, 8, 9 and 15 were done by the Unizar group using a high purity germanium detector (HPGe) at the Underground Canfranc Laboratory [11]. Measurements number 1, 3 and 4, were performed for the Unizar group by Shiva Technologies, France, using GDMS.

6 Expected performance

The well known $\beta\beta$ figure of merit,

$$T^{0\nu}_{1/2} \propto a\epsilon\sqrt{\frac{Mt}{b\delta E}} \tag{1}$$

although approximate, it clearly stresses the relevant experimental parameters determining the sensitivity of a $0\nu\beta\beta$ experiment: the isotopic abundance a, the detection efficiency ϵ, the source mass M and exposure time t, the normalized background rate b and the energy window δE determined by the energy resolution of the detector.

For the discussion of interest here, only the background b, the energy resolution δE and the detector efficiency ϵ could a priori be affected by the readout technology. The energy resolution is directly determined by the readout, as it is providing the energy information. The background of the experiment can be affected by all components of the detector close enough to the active volume, through their radiopurity, and, in particular, also the readout's radiopurity. Also, in an experiment like NEXT, the topological information provided by the readout is used to perform cuts on the data and reduce the background, therefore the tracking performance could also have an impact on sensitivity both through the background reduction achieved and the detection efficiency.

6.1 Tracking performance

In gas TPCs the ionization track of the particle along the medium can be registered with relative precision. This topological information can be used to identify and reject background events. In the detector configuration here proposed, the topological information differs from the physical ionization 3D track in two aspects: 1) the primary ionization charges *diffuse* along the drift, resulting in a somehow *blurry* version of the original track, and 2) the readout's anode is segmented in pixels of 1 cm^2, and therefore only a limited pixelized version of the track image is available for topological analysis. These two aspects must be properly taken into account when defining the discrimination algorithms. Moreover, the readout physics and electronics will impose a threshold and resolution in the charge detected in a given channel, and this may also have an impact on the quality of the topological information. This is briefly discussed below in 6.1.1.

For the purpose of the present document, the discrimination algorithms used rely only on 3 conservative categories of topological information of the event tracks. These algorithms are an extension of those initially developed in [24], where also the basic concepts are introduced and studied. The three categories are:

- **Fiducial cut**: the outermost cm of the active volume is treated as a veto, i.e. events depositing energy close to the edges of the field cage are rejected. This discrimination criterion rejects electron events associated with surface contamination (β emission) or with interactions in the wall materials.

- **Single "connection" cut**: this method aims at singling out only events with just one track or connection. The raw background at ∼2.5 MeV energies is largely composed by gammas interacting several times via Compton scattering in the gas. They are composed by more than one connection, and so they are easily rejected by this criterion. Unfortunately, $0\nu\beta\beta$ events may also yield multi-connection topologies (due to bremsstrahlung emission), and therefore this provokes an efficiency loss. Due to the wiggling nature of electron tracks of these energies (due to multiple scattering) the algorithm makes use of Graph Theory concepts developed in [24] to identify and number the connections of the event. Diffusion tends to merge connections that otherwise would appear disconnected. In order to reach some immunity against this effect, the algorithm plays with energy thresholds of neighboring pixels.

- **Two-blobs cut**: once events with just one connection are selected, those with 2 identifiable large energy deposits at the ends (blobs) are singled out. These blobs are the expected feature of an electron slowing down in the gas due to the increase of the dE/dx of electrons at lower energies. Two such blobs are expected in signal two-electron $0\nu\beta\beta$ events, while only one in average single-electron background events. The algorithm developed always assigns blob candidates to the events, and the main track between two of these candidates is drawn using the segments obtained in the connection method. Finally the charge of the blobs found at both ends are compared, since signal-events are expected to have similar energy depositions at the end of both electron tracks [25]. Features of the background events (δ-rays, random accumulation of charge, bremsstrahlung photons interacting close to the main track) may be misidentified as blobs.

The effect of the above mentioned criteria on both background and signal event samples have been carefully studied. The samples have been generated via simulation with Geant4 on a simplified geometry of the detector (see below 6.3). The effects of diffusion and pixelization are then applied to the simulated events. The above described algorithms are implemented in a ROOT-based C++ code that analyzes the simulated events. They are applied sequentially, and their corresponding efficiency (i.e. fraction of the total signal events that survive the cuts) is shown in table 3. On the other side, their effect on the background counts, or rejection factor, is shown, also sequentially, in table 2.

As background events have different sources, the rejection factor for each cut depends on the origin of the contamination. In such way, surface events will show a higher fiducial veto rejection factor since for these events charged particles emitted at the same time as photons can reach the sensitive detector volume. The one-connection cut will be more effective for ^{208}Tl events since they have a higher probability to suffer multicomptom interactions (more than one connection) in the RoI than ^{214}Bi events. Finally, the capability to identify one or two electrons in selected tracks does not depend on the origin of the event. In table 2 we show the effect in contributions coming from detector parts in contact with the sensitive volume and parts farther from it.

Table 3 shows the signal reduction due to the analysis. Signal events might be produced near detector walls and therefore be affected by the fiducial cut, but the effect producing the largest loss of efficiency is the Bremsstrahlung emission of photons. This emission may produce a second track in signal events, or loss of charge if the photon leaves the chamber. This happens in more than $\sim 40\%$ of the signal events. In background events, bremsstrahlung photons may produce a fake blob if it interacts near the main track.

Optimization of cuts could still yield larger rejection factors, at the expense of further efficiency loss. At the moment, priority has been given to keep a conservative approach to the topological cuts, by keeping a relatively small loss of efficiency. However, the work done up to now points to several possible improvements, although further studies are needed to quantify them. First, operation at high

Origin		Rejection Factor (F)		
		Fiducial Cut	Single Connection	Two Blobs Cut
Away from sensitive volume	Tl-208	1.3	45	6
	Bi-214	1.1	15	6
In contact with sensitive volume	Tl-208	5	45	6
	Bi-214	50	15	6

Table 2: Effect of each discrimination cuts sequentially applied on elements in contact with the sensitive Xe volume (like the readout) and away from it. Values shown here are mean values obtained from different simulations and analysis. Rejection factors of a cut are expressed in relation to the previous cut surviving events.

	Efficiency			
	RoI	**Fiducial Cut**	**One connection**	**Two blobs**
$\beta\beta0\nu$	0.92	0.79	0.37	0.27

Table 3: Effect of the different cuts on the signal efficiency (surviving events versus total events), for a region of interest (RoI) corresponding to 3% of $Q_{\beta\beta}$. Cuts have been sequentially applied.

pressure pure Xenon imposes a large diffusion on the primary ionization cloud. This diffusion has a definite effect on the quality of the topological information as is illustrated below in subsection 6.1.2. The higher the diffusion the more difficult the tracks are to separate and blobs to identify. Work is ongoing to quantify this in terms of the rejection factor, but preliminary simulations assuming smaller electron diffusion [24] points to an extra factor of $\sim$10 in background rejection. Second, attempts to reduce Bremsstrahlung emission would certainly yield improved sensitivity by enhancing the cuts' efficiency. This could be achieved by adding low-Z additives (e.g. Ne) to the Xe. These two points, together with other reasons commented later on, **strongly motivates the use of gas additives to the Xe** as an improved stage of the baseline design in pure Xe here considered. Once again, keeping a conservative approach, we do not adopt these options in our baseline design, as they need further work, and we will consider the cuts and numbers presented before in the background model and sensitivity study developed later on. Nevertheless, we will discuss the option of using a Xe mixture below in section 10.2.

Some other improvable aspects regarding the topological cuts are listed in the following and should drive future work:

1. Continue the study on the way the charge is deposited along the track at different pressure conditions, in order to try to extract further topological information from dE/dx.

2. Try to use topological information to identify events interacting near the readout or the cathode. Preliminary results are very promising. If successful this could substitute t_0 information to perform the fiducial cut (see section 10).

3. Study topological signatures that could allow the identification of bremsstrahlung photons interacting near the main track.

4. Study the Čerenkov emission of electrons as a possible distinctive signature between $0\nu\beta\beta$ and background events (discussed in section 10).

6.1.1 Pixel charge threshold

The simulations to generate the rejection factors and efficiency numbers shown in tables 2 and 3 have been used to study the effect of non-zero threshold in the detectable charge per pixel. By removing from the analysis pixels below a given threshold energy, we have observed that the cuts start losing both efficiency and rejection power steadily for thresholds energies above a certain value, while there is no effect below it. This value is of ~ 10 keV for pixels of 1 cm^2, and should be perfectly achievable by the pixel readout of the proposed microbulk plane.

6.1.2 Effect of Diffusion

The high diffusion coefficient in pure Xe implies a wider ionization electron cloud. The spreading of the charge makes the tracking more complicated since more pixels are hit and the charge per pixel is lower. It strongly depends, moreover, on the distance to the readout. Figure 7 shows three of the simulated signal events which have survived all the analysis cuts. It can be appreciated how at high z it is more difficult to identify events as *one track* instead of two depositions (which could be caused by background events).

One of the consequences of diffusion is that tracks produced by different electrons (as for example, those caused by multicompton interactions) merge and fake two electron tracks (see an example in figure 8). To eliminate them, analysis parameters have to be adjusted to *clean* the connection; however, this will also affect signal events and imply an efficiency loss (see figure 9), more pronounced at larger distances to the readout. Another consequence of diffusion is that the energy deposition at the end of the track (*blobs*) spreads over a large radius making it more difficult to distinguish this deposition from the energy deposited at other points of the track. In figure 9 a large population of simulated signal events is plotted with indication of the z-coordinate. Depopulation in the edges is the effect of the fiducial cut. A slight z-dependence of the cut's efficiency is appreciable, indicating that, even with the conservative choices made to define the cuts, there is an effect of the diffusion on the quality of the topological information. As commented previously, the use of gas additives to the Xe that would decrease the diffusion would improve the power and efficiency of the topological cuts.

6.2 Energy resolution

As mentioned before in section 4.1, microbulk Micromegas have been shown to achieve an energy resolution equivalent to 2% and 3% FWHM at $Q_{\beta\beta}$ for 5 and 10 bar respectively working in pure high pressure Xe. Although measurements with high energy alphas are available, these values rely on simple $\propto E^{1/2}$ extrapolation from the low energy (22 keV and 60 keV gammas) measurements on small scale (3 cm diameter) readouts. In realistic NEXT conditions, with ~ 2.5 MeV electron tracks extending along ~ 30 cm, several features need to be checked not to further contribute to the energy resolution. We discuss them briefly in the following, although experimental demonstration of energy resolution in realistic NEXT conditions (electron extended tracks) is a must and it is the goal of the NEXT-1-MM program.

- Electrons may gain or lose extra energy from the drift field along their ionizing track, depending on the starting and ending point of their track, and the intensity of the drift voltage. This translates into an extra fluctuation in the energy deposited in ionization. As computed in [26], the degradation to

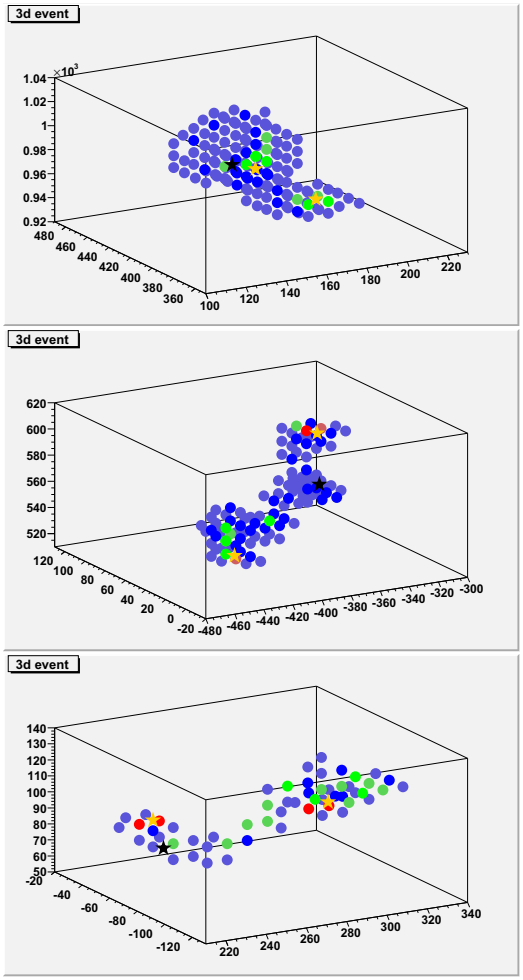

Figure 7: Simulated signal events at different z position (vertical axis). Black star marks the vertex while yellow stars indicate the end of both electron tracks. Charge spreading due to diffusion is more important for events produced near the cathode.

the energy resolution due to this effect is ~ 0.5 % FWHM for a drift field of $\sim$0.1 kV cm^{-1} bar^{-1} (being linear with it). This imposes a maximum drift field in order to keep good energy resolution.

- Electron tracks in NEXT travel $\sim$30 cm although following a wiggly trajectory. This means that the energy information must be extracted from a mesh area which is a factor $\sim$10 larger than the one used in the previously stated measurements. The contribution to the energy resolution by the capacitive noise ($\propto C^{1/2}$, being C the electrode capacitance) will be a factor ~ 3 larger. The effect on the energy resolution depends on the relative importance of this contribution in the current energy resolution measurements, and could perhaps be reduced by optimization of front-end electronics. In the worse case, a relative increase in gain of at most the stated factor or ~ 3 would be needed to keep the signal-noise ratio and therefore to keep the same energy resolution.

- Moreover, the time spread of the signal will be also longer. This may impose constraints on the front-end electronics (shaping or sampling times).

The mentioned effects do not necessarily constitute unavoidable extra contributions to energy resolution, although they need to be probed experimentally in NEXT-1-MM. On the other hand, there are prospects to improve the previous stated values as commented later on in section 10. For the sake of sen-

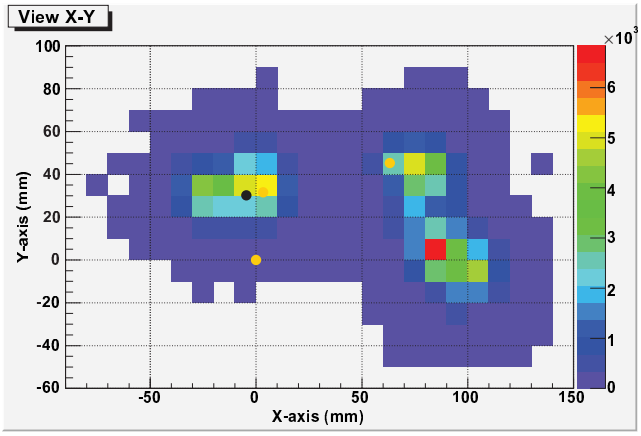

Figure 8: Effect of diffusion on pattern recognition: two independent deposits of energy are joined because of the high diffusion in xenon

sitivity estimation in the following paragraphs, we consider a 2.5% FWHM as a realistically achievable value for our baseline configuration at 8 bar.

6.3 Background model

An appropriate background model for NEXT should include as many background sources as possible, together with a description of the geometry of the detector and a simulation of its response as faithful as possible. Searching the always needed compromise between resources, manpower and time available, on one side, and accuracy and usefulness of the results, on the other, we have made some simplifying assumptions to build up a reasonable background model to be used for the present proposal. These assumptions are explained and justified in the following.

As anticipated in section 5, all external sources beyond the detector vessel are excluded from our background model. This is justified only if the specifications expressed in that section for the shielding are met, namely: 1) that the shielding is thick enough to stop all relevant external gamma radiation down to negligible levels for NEXT, 2) that the "clean" innermost part of the shielding is thick enough to stop any radioactivity from the outer part of the shielding, and that it is as clean, at least, as the vessel material itself. Moreover, we identify this innermost material (high purity copper) with the vessel material and therefore only the innermost 3 cm of shielding/vessel are representative and are included in the background model.

Moreover, we have made an effort to identify as many elements as possible of the inner components of the detector, their material, quantity, and potential radiopurity, as they will be unavoidable sources of background. Only decays capable of populating the $Q_{\beta\beta}$ area have been considered, namely ^{208}Tl, from the ^{232}Th natural chain, and ^{214}Bi from the ^{238}U chain. The simulated geometry, a view of which is shown in figure 6.3, is a simplified version of the one described in section 4, including only the main media of geometrical relevance: the copper vessel parts (body, endcaps and flanges), the field cage teflon support and copper rings, the microbulk (simplified into a single plane of contamination), cathode, and a quartz plane representing the PMT contamination. Simulated data from some prototype geometrical lo-

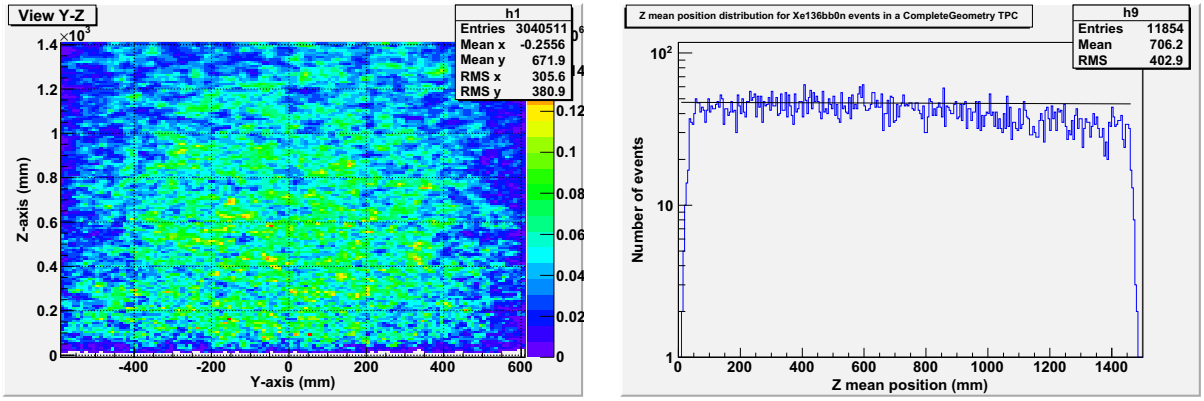

Figure 9: Loss of efficiency due to higher diffusion at high z. Events passing all the cuts have been plotted: general YZ view (left) and z position (right) where a straight line has been drawn to guide the eye.

cations has been generically generated (vessel, field cage, cathode, readout). The contribution of smaller elements not included in the geometry (e.g the field cage resistors or the flat cables) are estimated by taking the data simulated from the prototype location that matched most the geometry of that element, and properly renormalizing it using its mass and radiopurity. For example for the resistors, the simulation from the field cage was used. We took care that in these procedures the approximations performed went always in the conservative direction. For example, for the flat cables estimation we used the data simulated from the readout plane, although the flat cable geometry is partially attenuated by copper from the endcap.

In this way, the following list of elements have been identified and their contribution estimated, the amount/mass of each of them being indicated in table 4:

- The cylindrical body of the copper vessel (3 cm thick), flanges and the 2 torispherical endcaps (only the innermost 3 cm is taken into account).
- The cylindrical field cage composed by copper strips imprinted in teflon.
- The cylindrical teflon piece supporting the drift cage and isolating the high voltage from the vessel (2 cm thick).
- The high optical transparency copper mesh at the cathode.
- 130 SMD resistors for the field cage
- Silver paste to do the the electrical connections of the resistors and the field cage rings.
- The microbulk Micromegas readout planes.
- Epoxy to attach the micromegas to its support.
- 50 flat cables and 210 copper pieces (tensors) to extract the signals form the Micromegas pixels to the feedthroughs.

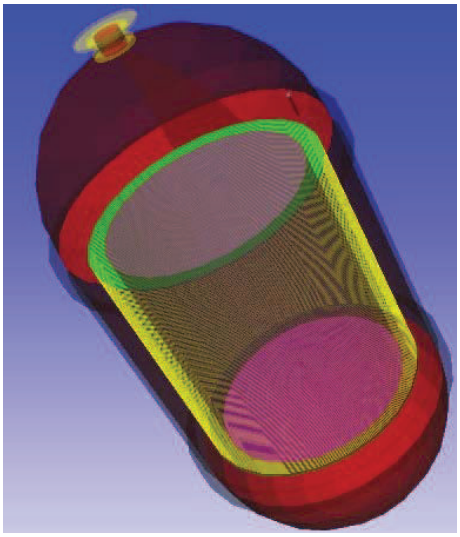

Figure 10: General view of the simplified geometry used in the Geant4 simulations.

- 50 PLC interface pieces for the contact connections.
- The copper support pieces for the microbulks.
- 49 PMTs of the t_0 readout
- 7 quartz windows.
- The copper frame of the cathode and the copper bar that give voltage to the cathode.
- Extra protective teflon pieces above the cathode and composing the HV feedthrough.

The contribution of each of these elements, both by their ^{208}Tl and ^{214}Bi contaminations, have been singled out. The results, included the filtering resulted from the topology cuts described in a previous subsection, are shown in the table 4. The second column indicates the radiopurity level considered for each material, linking to the corresponding entry of table 1. Columns three and four indicate the contribution of ^{208}Tl and ^{214}Bi respectively, in units of counts per year. For ^{214}Bi they include all counts in the peak, while for ^{208}Tl they include the counts in a region of 3% around $Q_{\beta\beta}$. The fifth column sums both contributions in the standard units of counts keV^{-1} kg^{-1} y^{-1}.

Most of these contributions are upper limits, as they are derived from measured upper limits to their radiopurity. The sum of all items, irrespectively of whether they are upper bounds or not, is indicated in the "pessimistic total". A more realistic estimate allows us to expect lower values for some of the elements with upper limits. A typical example is the contribution from the microbulk readout, which appears artificially high because it is based on an upper limit from a HPGe measurements of very light samples [11]. Although more sensitive measurements are needed, it is realistic to expect that the actual contamination will be much lower (an estimation using contamination of the bulk raw materials, copper, kapton and epoxy, gives values 100 lower than the upper limit used). The "realistic total" thus excludes this contribution from the sum, and halves all other contributions coming from upper limits. The only contributions not coming from upper limits and amounting to a significant fraction of the background are the PMTs and the field cage resistors.

Origin	Activity entry	**c/y**		**(c/keV/kg/y)$\times 10^{-4}$**
Simulated	(from table 1)	Tl208	Bi214	Total
PMT$\times$49	#26	0.43	0.02	0.75
Readout	#9	< 1.1	< 1.1	< 3.7
PTFE electrical protection (200kg)	#12	< 0.26	< 0.02	< 0.46
Vessel(body + end caps + flanges) (3.4 T)	#3	< 0.85	< 0.13	< 1.63
Resistors	#24	0.14	0.010	0.26
Cathode(2.12kg)	#3	< 0.020	< 0.028	< 0.08
Field Cage (102 kg)	#3 and #12	< 0.007	< 0.007	< 0.02
MM copper supports	#3	$< 1.8 \times 10^{-3}$	$< 8.0 \times 10^{-3}$	< 0.013
Epoxy (10 g)	#17	9.58×10^{-3}	1.40×10^{-3}	1.49×10^{-2}
Quartz windows (7 pc)	#27	3.46×10^{-3}	1.68×10^{-3}	6.97×10^{-3}
HV PTFE protection (0.40 kg)	#3	$< 3.96 \times 10^{-6}$	$< 3.51 \times 10^{-7}$	$< 5.29 \times 10^{-3}$
PLC connection pieces (70 pc)	#16	$< 8.45 \times 10^{-6}$	$< 8.45 \times 10^{-6}$	$< 2.29 \times 10^{-3}$
Kapton flat cables (70 pc)	#10	5.50×10^{-6}	2.5×10^{-5}	4.20×10^{-3}
Polyamide PCB (210 pc)	#10	1.2×10^{-5}	1.9×10^{-5}	4.30×10^{-4}
Silver (15 g)	#20	$< 6.35 \times 10^{-5}$	$< 5.61 \times 10^{-5}$	$< 1.62 \times 10^{-4}$
Total (pessimistic)		< 2.8	< 1.3	< 6.9
Total (realistic)		1.14	0.12	1.7
Total (improvements)		0.25	0.015	0.3

Table 4: Contributions to the background from every element of the detector after discrimination cuts applied. See text for explanation.

The third total indicated ("improvements") is not based on the baseline design simulated, and illustrates a guess based on the assumption that one or more of the improvements beyond the baseline design discussed later on in section 10 could yield a background improvement of a factor ~ 6 beyond the "realistic" baseline background level (by means, for example, of avoiding the use of PMTs for t_0, or by improving cuts rejection power by the use of Xe mixture with lower diffusion)

6.4 Sensitivity

With the experimental parameters justified above, mainly background, energy resolution and efficiency, the expected sensitivity to $0\nu\beta\beta$ for our proposed detector for NEXT-100 has been computed. The calculation is done is the following way: 10^3 toy Monte Carlos of the background around $Q_{\beta\beta}$ are performed using a realistic spectral distribution and experimental exposure. The likelihood function is built upon the simulated counts using the signal (approximated by a gaussian of the required width) and the background models. The 95% CL upper limit to the signal intensity is then computed in the standard way from the likelihood function, but for the cases of very low background, for which the limit is obtained by integration of the Bayesian posterior probability. The sensitivity is defined as the average of the upper limits obtained over the 10^3 toy Monte Carlo performed. This method is good enough for our purposes, and in particular allows to include spectral information in the analysis. More theoretically rigorous approaches could be followed, like the Feldman-Cousins unified prescription, however at the expense of more computation complexity, specially if spectral information is to be added to the models.

The result is plotted in figure 11 for both 1 (left) and 5 (right) years of data taking (80 and 400 kg y respectively) versus the value of the energy resolution, and for the three background scenarios defined in

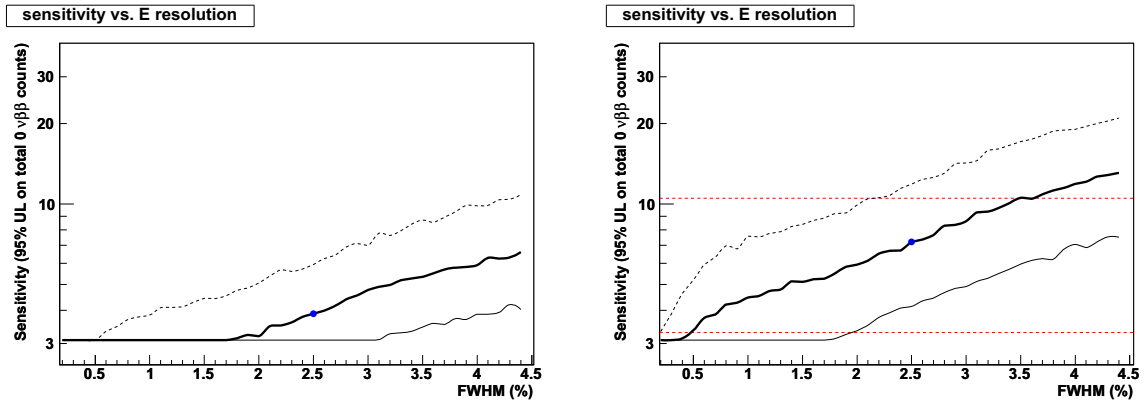

Figure 11: Estimated sensitivity in terms of the upper limit to the signal intensity in total observed counts versus energy resolution. On the left, for one year of data taking (80 kg y of exposure) and on the right for 5 years (400 kg y). Please note that the y-axis is expressed in total signal counts in the exposure considered (1 year on the left, 5 years on the right). The three background scenarios commented in the text are shown: pessimistic (dashed line), realistic (thick solid line) and improved (thin line). The two dashed horizontal lines in the plot on the right correspond to the expected $0\nu\beta\beta$ intensity for a $m_{\beta\beta} = 100$ meV using two extreme different NME calculations (see text). The lower line also corresponds approximately to the expected signal for $m_{\beta\beta} = 50$ meV with a favorable NME. The blue dot would correspond to our baseline configuration with 2.5% FWHM energy resolution.

the previous section. The two dashed horizontal lines in the plot on the right correspond to the expected $0\nu\beta\beta$ intensity for a $m_{\beta\beta} = 100$ meV using a favorable ($M^{0\nu} \sim 4.2$ [27]) and not favorable ($M^{0\nu} \sim 2.1$ [28]) Nuclear Matrix Element calculation for ^{136}Xe. The lower line corresponds also approximately to the expected signal for $m_{\beta\beta} = 50$ meV with the favorable NME.

In figure 12 the sensitivity, this time expressed in the corresponding half-life of the $0\nu\beta\beta$ decay, is plotted versus exposure time. The two horizontal red dashed line have the same meaning as in figure 11. As before, the thick solid line represents the baseline design of 2.5% FWHM with the realistic background model. The pessimistic model is also shown (dashed black line) to illustrate the importance of keeping under control the radiopurity of the components studied in section 6. The blue set of lines represent different scenarios of improvements beyond the baseline. The solid thick blue line corresponds to the improved background scenario of table 4 which, we remind, it is only a factor $\sim$6 better than the realistic one. The thin blue line corresponds to the realistic background case but with an eventual improvement in energy resolution down to 1% FWHM, possible in some of the improved scenarios discussed in section 10. Both improvements are roughly equivalent in terms of sensitivity. The combined improvement in background and resolution does yield an extra step in sensitivity but only when sufficient statistics ($\gtrsim$ 3 years) is gathered.

The quantification of these improvements is a bit arbitrary at this point, but they are qualitatively well founded in realistic prospects discussed in section 10, and to some extent they are even conservative. Indeed, a enhanced stage of the detector design implementing one or more of the improvements considered there could potentially lower the energy resolution to below 1% FWHM, and/or reduce the background level by factor certainly more than the 6 here considered, provided the R&D issues commented in section 10 are successfully developed. This improved stage would naturally fit in time at the 2-3 years of operation of the first baseline detector, according to figure 12.

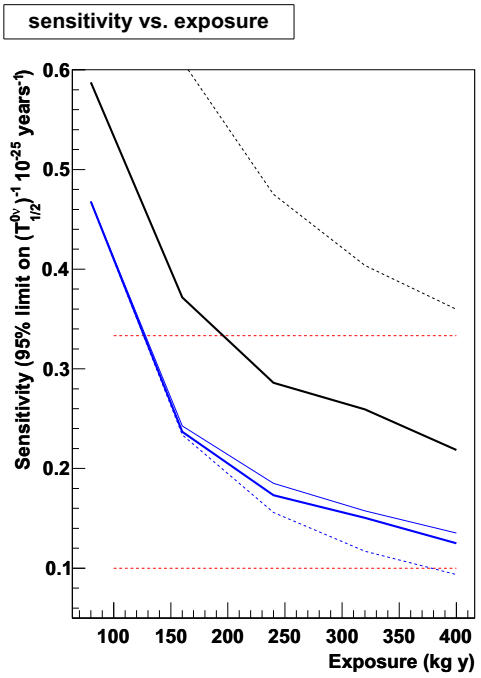

Figure 12: Expected sensitivity versus exposure. The two horizontal red dashed lines have the same meaning as in figure 11. The thick solid line represents the baseline design with 2.5% FWHM and the realistic background model, and the dashed line with the pessimistic background model. The blue lines result from different improvements over the baseline design commented in the text: improved background scenario (thick blue), improvement in energy resolution to 1% FWHM (thin blue line), both improvements together (dashed blue line).

Therefore, and although not considered in this study, more aggressive scenarios could be justified, based on more optimistic assumptions for the mentioned improvements. Let us mention especially 1) the possibility of much powerful software cuts derived from successful operation in a low diffusion Xe mixture, or 2) the possibility of increasing the efficiency of cuts by using low-Z additives to the Xe, or by successfully identifying signal topologies that are at the moment lost by diffusion.

7 Operation issues

Without being exhaustive, in this section we briefly comment on some aspects regarding the operation of the proposed detector configuration. Firstly, we focus on maintenance issues derived from the use of Micromegas as NEXT-100 readout. Secondly, we propose a calibration protocol for the detector.

7.1 Maintenance

The modular design proposed for the Micromegas readout in section 4, is well suited for relatively easy replacement of single modules in case of malfunctioning. The module support mechanics, based on independent copper pieces, as well as the system of signal extraction via contact connectors, is designed to allow for independent access to each module, and eventual replacement if needed. Nevertheless, the replacement of a module implies the evacuation and opening of the detector vessel, and subsequent closing and pumping, adding up to a rather cumbersome operation whose frequency we want to minimize.

One of the concerns when working with charge readouts (and more specifically with MPGDs) is the occurrence of discharges, and especially of damaging ones (see below section on risks 9). They can damage the front-end electronics, if not properly protected, or the readout itself. Although Micromegas has shown an outstanding behavior in high pressure pure Xe with respect to other MPGDs, the absence of quencher always lowers the limiting point where instabilities and discharges start appearing. Fortunately,

the current experience with microbulk operation in pure Xenon tells us that the limiting discharge that eventually appears is not one that damages the readout permanently, but it does produce a temporary short-circuit between the mesh and the affected pixel. This short-circuit renders the affected module inoperative (at least only the part of the module sharing the same mesh electrode). This situation is cured just by exposing the readout to air[3] (probably other electronegative gas would also work), without needing to dismount or replace the readout. In any case, the occurrence of such event, even if not needing the replacement of a module, would however disrupt the normal NEXT data taking operation, as the detector vessel would need to be evacuated (although not opened). To minimize the consequences of such situation we propose to equip the front-end electronics with the possibility of disconnecting at will any chosen pixel from the readout chain. This would allow to isolate the short-circuited pixel from the system at the outside of the vessel, allowing to apply voltage to the mesh at that point again, with no alteration to the detector. Running with a number of inoperative pixels is perfectly possible with totally negligible consequences to the performance of the detector, be it efficiency, topological rejection power or even energy resolution. Detailed simulations are needed to determine this number, but preliminary considerations point at least to about $\sim$25. This leaves a rather comfortable margin against this kind of disruptive events. Once the number of inoperative pixels reaches this number, the NEXT operation protocol should include a gas evacuation and curing of the affected pixels.

Of course, experience with small prototypes like NEXT-1-MM is needed to better evaluate the plausibility and extent of these problematic situations. Moreover, in the possible future scenarios discussed in section 10 contemplating the use of quenchers, this risk would be greatly diminished.

7.2 Energy Calibration

For an experiment like NEXT with very demanding requierements on the energy measurement, a key element for the success of the experiment is to have an adequate method for the energy calibration of the detector. The calibration method should ideally fulfill the following conditions: the energies for the calibration should cover the full relevant energy scale defined by the interesting physics process. The method should also allow to scan at least the full xy-plane although additional information about the z-position is desirable. And finally the calibration process should neither distort the detector performance e.g. by introducing solid objects within the sensitive volume, nor should interrupt the data taking for too long so that the calibration can be repeated frequently. For a pixelized detector, in which the energy deposition per pixel for the case of NEXT can be up to 200-300 keV, there exist two calibration methods which fulfill the above mentioned conditions: The ^{83m}Kr method and the activated xenon method.

7.2.1 ^{83m}Kr method

The energy calibration of a TPC with ^{83m}Kr is a well established method. It was developed for ALEPH [29] but later used also for the NA49 [30] and STAR [31] chambers. The system is based on introducing a foil doped with ^{83}Rb into the gas system. ^{83}Rb decays with a half-life time of about 86 days into ^{83}Kr under the emission of various X-rays (see figure 13).

This decay is interesting since most of the decays occur via the metastable energy level, ^{83m}Kr, at 41.5 keV which has a long life time of about 2 hours, enough so that the Kr gas gets distributed within the chamber. On the other hand the half-life time is short enough so that after removing the ^{83}Rb source from the gas flow, the normal data taking can be started again soon. From the 41.5 keV energy level the decay to the ground level occurs via the energy level at 9.4 keV leading to a spectrum shown in figure 13

[3] sometimes it disappears spontaneously after some time without voltage

Xe Isotope	Abundance (atom %)	Reaction Mode	Cross-section (barn)	Daughter Product	Decay Mode	Decay Half-life	E_γ[4] (keV)	Rate[5] (Bq/kg) t = 1 day
^{124}Xe	0.09	^{124}Xe(n, γ)^{125m}Xe	28	^{125m}Xe	IT	57 s	252.8	<1e-6
		^{124}Xe(n, γ)^{125}Xe	147	^{125}Xe	β^+,EC	17 hr	188/243.4	100
		^{125}Xe $\rightarrow^{125}$ I	—	^{125}I	EC	59.4 d	35.5	1
^{129}Xe	26.4	^{129}Xe(n, n′)^{129m}Xe	1.6	^{129m}Xe	IT	8.9 d	236.1	100
^{131}Xe	21.2	^{131}Xe(n, n′)^{131m}Xe	1.3	^{131m}Xe	IT	11.8 d	163.9	100
^{132}Xe	26.9	^{132}Xe(n, γ)^{133m}Xe	0.05	^{133m}Xe	IT	2.2 d	233.2	1
		^{132}Xe(n, γ)^{133}Xe	0.4	^{133}Xe	β^-	5.2 d	81.0	10
^{136}Xe	8.87	^{136}Xe(n, γ)^{137}Xe	0.23	^{137}Xe	β^-	3.8 m	455.5	<1e-6
		^{137}Xe $\rightarrow^{137}$ Cs	—	^{137}Cs	β^-	30.1 y	661.6	1e-3

Table 5: Overview about the reaction modes, decay producs, half-life times, energies and rates for 1 kg of activated natural xenon. Taken from [33].

[31]. This plot is a simulation for Ar:CO_2 50:50. Since the absorption length of the x-rays and the size of the readout pixels is affecting the recorded spectrum, the lines and their corresponding intensities will change for xenon at 10 bar. However, the energy range is not affected by this.

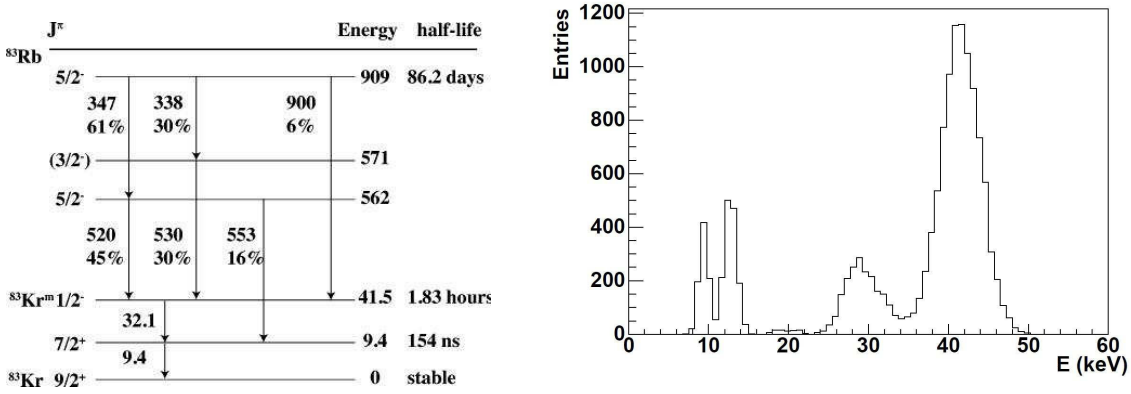

Figure 13: Left: energy level diagram (in keV) for the ^{83}Rb decay [32]. Right: simulation of a spectrum obtained with ^{83m}Kr in Ar:CO_2 50:50. An energy resolution of 6 % (σ) was assumed [31].

The main drawbacks of this method might be that the maximal deposited energy is only 41.5 keV and that another gas, Kr, is introduced into the enriched xenon.

7.2.2 Activated xenon method

For the calibration of liquid xenon detectors a method based on neutron-activated xenon was recently developed [33]. The idea is to produce metastable xenon by fast neutron activation of xenon, ^{128}Xe and ^{130}Xe, and to use afterwards the γ-rays emitted from the daughter products for the calibration. In table 5 an overview about the energy lines and the half-life times for the case of an activation of 1 kg of natural xenon by ^{252}Cf is shown.

Energy depositions between 35.5 keV and 243.4 keV are available covering the interesting energy range for a pixelized readout. A main drawback of this method is the long half-life time of many of the daughter products. Also the rate might be limited when instead of natural xenon enriched xenon is used for the activation since in this case the fraction of ^{128}Xe and ^{130}Xe will be reduced in the gas. On the other hand the use of enriched xenon for the activation is desirable since the detector mass should not be

Concept	Price €/ud.	Quantity ud.	Price €	Subtotals k€
Material / Equipment				
Micromegas	2000	60	120000	
Flat cables + FT	300	120	36000	
			Subtotal k€	156.00
Items related to the vessel endcap				
Lateral copper stuffing	12	426	5112	
Thick copper support structure	12	1120	13440	
Teflon stuffing	5135	1	5135	
Hardware copper	15	35	525	
Teflon gaskets	75	5	375	
Tubes copper	225	20	4500	
Flange copper	74	60	4440	
3FlangeFT copper	441	20	8820	
			Subtotal k€	42.35
Manufacturing costs				
General copper machining	Assumed by NEXT groups' workshops or LSC			
Tubes EBW	600	40	24000	
Teflon stuffing machining	300	1	300	
Thick copper structure machining	6000	1	6000	
			Subtotal k€	30.30
			Total k€	228.65

Table 6: Estimated costs for the microbulk Micromegas charge readout.

diluted over time. Although this method was developed for a liquid xenon detector, it is also applicable to gaseous xenon.

8 Costs

We give here some costing information regarding the technological option proposed. Only items composing the readouts themselves (microbulk modules, PMTs, quartz windows, signal cables and connectors) or induced on the vessel design because of the implementation of the readouts (copper outlets and their welding, feedthroughs, fabrication costs, etc...) are included. The fabrication of the copper vessel itself and the field cage are not included here (see [34]).

In table 6 the Micromegas readout cost is estimated together with its implementation in the anode endcap of the vessel. Similarly in table 7 the cost of the t_0 readout (PMTs and quartz windows) is estimated as well as the costs of integrating them in the cathode endcap. The break-up of the estimations are rather complete and although some items are costed by real offers by companies other items have been estimated and could vary. In particular, by ordering large quantities of identical pieces (Micromegas,...) final prices could get somehow lower than the ones quoted.

Concept	Price €/ud.	Quantity ud.	Price €	Subtotals k€
Material / Equipment				
Fused Silica Quartz	1815	7	12705	
PMT	1360	49	66640	
			Subtotal k€	79.34
Items related to the vessel endcap				
Teflon over the cathode	36100	1	36100	
Support Teflon copper	677	1	677	
Tube copper	506	7	3542	
Flange copper	74	10	740	
Hardware copper	179	9	1611	
Teflon gaskets	110	2	220	
Stuffing copper	12	498	5976	
Stuffing Teflon	722	1	722	
Cathode Copper	2720	1	2720	
Copper grid	872	2	1744	
			Subtotal k€	54.05
Manufacturing costs				
General copper machining	Assumed by NEXT groups' workshops or LSC			
Tubes EBW	600	7	4200	
Cathode machinning	300	2	600	
Teflon machining	900	1	900	
			Subtotal k€	5.7
			TOTAL k€	139.10

Table 7: Estimated costs of the t_0 scintillation readout

9 Risks and contingencies

All options have their risks and trying to anticipate them allows to devise possible contingency plans. In the following we enumerate some possible risks of this proposal (primarily those directly linked with the Micromegas readouts), and we discuss them briefly trying to assess their plausibility and eventual impact and to define to some extent the basis for possible mitigation plans for each of them. We must keep in mind, even if we have opted for conservative options as much as possible, that we are doing research at the limit of techniques in several aspects and it is very likely that we face surprises.

- The total area of microbulk here proposed will be the largest amount of microbulk readout ever manufactured, so one could not totally exclude unforeseen circumstances at fabrication, with could produce, for example, delay in their production. In answer to this concern, we have to consider that microbulk Micromegas, although a relatively new technique, have already gone through moderately intense cycles of developments and application. Throughout the second phase of the CAST experiment [35, 36, 37], in which microbulk Micromegas are being used, more than 15 readouts of 50 cm^2 active area (and 500 cm^2 total printed kapton area each) have been manufactured at CERN, with sustained feedback from detector users to fabrication technicians at CERN to allow for improvement and consolidation of the fabrication processes. Already for the Unizar R&D program (mostly for NEXT-1-MM) microbulk readouts amounting to a total active area of 1500 cm^2 with already very similar characteristics as the one needed for NEXT-100 have been manufac-

tured. This is a non-negligible fraction of the area of NEXT-100, and although the fabrication of the NEXT-100 readout will be undoubtedly an important and difficult task, this reduces the probability of unpleasant surprises in the process. Finally, the group eventually in charge of microbulk fabrication, R. de Oliveira's workshop at CERN, is a world leader in MPGDs development and fabrication, and has specific experience in large scale fabrication for concrete applications (the typical example being the $\sim$10 m^2 of bulk Micromegas built for the T2K TPC)

- Although operation up to 10 bar in pure Xenon has been demonstrated experimentally as commented in previous sections, this has been achieved in small setups and short measurements periods. We know that the higher the operating pressure, the closer the operation point of the Micromegas is to the limit of stability and the onset of discharges. To operate such a large area of readout and for such long periods as required in this operation point will be challenging. Regarding long periods of operation, the experience in CAST provides a good reference for year-long campaigns of uninterrupted operation with microbulk detectors at gains above 10^4. Beyond this, several aspects are considered as mitigation of this risk. First, default operation at the lower pressure of 8 bar gives some safety margin. Second, some degree of tolerance with discharges is achieved by the possibility of disconnecting the affected pixel from the front end electronics from the outside, as discussed in a previous section. Third, addition of a fraction of Ne to the Xe improved the maximum gain achieved by the Micromegas (and probably the energy resolution) and therefore the range of safe operation (we refer to appendix A for details on Ne-Xe data). Finally, as part of the overall philosophy of our proposed staging scenario, ongoing R&D (some of it done by NEXT groups) on Micromegas readouts may provide further solutions to this shortcomings (use of quenchers, improvements in the Micromegas geometry itself, developments on discharges protection via resistive coatings). All these reasons provide good prospects to deal with possible risks related to high pressure operation of Micromegas, in any case, due to the importance of this issue we consider very important that full operation experience is demonstrated in an intermediate scale prototype.

- Another conceivable risk is that our extrapolation on the energy resolution in realistic NEXT conditions fails due to factors unforeseen in our discussion of section 6. Although our estimation contains some degree of conservativeness, in case of an eventual worsening of the final energy resolution achieved, it could in part be also compensated by better results on background according to the combined effect on the sensitivity as was quantified in 6.4. In any case, R&D work is ongoing to further improve energy resolution and our prospects is that better values than the baseline ones will eventually be reached and implemented in a second stage, following one or more of the lines described in 10.

- Finally, another risk would be that one or more of the contributions in the background model developed in 6 resulted underestimated, or that new contributions appear that were not contemplated, consequently leading to a larger background level than expected and a diminishment of the sensitivity. The first of these options appear improbable, provided an exhaustive program of material screening is performed in NEXT, to detect any sample not complying with the radiopurity specifications or to exclude contaminations during manipulation, for example. For the level of detail of this document, and the relative simplicity of the baseline design proposed, the study performed on the materials entering the geometry is relatively complete and the possibility of surprises in this area are reduced. Moreover, most of the contributions to the background model come from materials with upper limits on their radiopurity, which adds an extra safety margin. On the other

hand, a very real possible source of background that was not considered in out model is radon, as was largely commented in section 5. The study of radon and its control in NEXT must be a priority for the collaboration.

As an overall measure of risk mitigation we propose a general course of action which includes sustained R&D activities to explore and improve diverse aspects of the experiment. Keeping an open design capable to incorporating one or more of these improvements as they become established is probably the best long-term strategy for risk mitigation. Some of the improvements that may become a reality in the near future are commented in the next section.

10 Foreseeable improvements

Although we acknowledge the merit of taking decisions on the readout technology and of reducing the phase space of possible options, for the sake of optimization of resources, we consider that the current information does not allow for a complete definition of the NEXT-100 at this time. Moreover, to close the door to the possibility of accommodating improvements in our setup that may appear evident in the near future can be a serious shortcoming. Although this document has presented, as a baseline choice, a conceptually well-defined design for NEXT-100, the course of action that we propose for the collaboration is to test this choice in intermediate detectors and, at the same time, keep exploring alternative options or enhancements that could provide clear improvements in subsequent stages of the experiment. We describe our proposed staging strategy in the next section. These possible enhancements can also be the basis for mitigation plans in the case some of the risks enumerated in the previous section become real. In the following we select a few issues that could complement, substitute or improve some of the aspects of the baseline design, which we consider they have large potential if ongoing development work yields successful results, and that NEXT should monitor closely.

10.1 Alternative measurement of primary scintillation

Being the PMTs an important contribution to the background, to search for alternative options to measure the primary scintillation is an obvious way of improvement of our baseline design. In the MAGIC approach in which the photosensors at the cathode are only for t_0 measurement, and therefore with less requirements regarding homogeneous response/coverage than in the ANGEL scheme, options considering gaseous photomultipliers or photosensors coupled to scintillating bars become plausible alternatives.

10.1.1 Gaseous Photomultipliers

A low-cost and potentially radiopure alternative to commercial PMTs might be gaseous photomultipliers or photon counters. These devices underwent a significant advancement in the last years caused by the improvements of micropattern gas detectors (MPGDs). A possible detector concept could consist of a quartz window transparent to DUV light followed by photocathode e.g. coated with CsI. This coating can be applied to the surface of a MPGD as for example a THGEM. By chosing an adequate electric field configuration, the electrons released on the photo cathode are guided into the holes where a charge amplificaton takes place. To increase the maximal gain of the system a cascade of two or three THGEMs is normally used. The advantage of this approach is that large areas can be covered very cost effectively. A research group from Canada is currently preparing a large module based on photo counters which is designed to stand 10 bars [38]. In addition to be sensitive to single photons, a research group from

Coimbra found promising results for the achievable energy resolution for a photon counter based on a microstrip plate (MSP) readout [39]. Finally, the group of CEA/Saclay is also developing very sensitive UV detectors based on CsI-coated Micromegas planes with very promising results (Forfire project).

10.1.2 MPPCs

Multi Pixel Photon Counters (MPPCs) are also an interesting alternative to the classical PMTs. While they have a reasonable price per unit, they have the disadvantage of being available only in small sizes of up to 3x3 mm^2, having a large noise rate of several hundred kHz and not to be directly sensitive to the scintillation light of xenon. A research group from the University of Bern is working on a way to overcome the last point [40]. They presented the idea to couple the MPPCs to TPB (tetraphenyl-butadiene) doped bars to shift the deep UV light to the blue region where the MPPCs have a reasonable detection efficiency. By covering both ends of the bar with MPPCs also the noise problem might be overcome by requiring a coincidence in both sides. Beside of the fact that such a system would be by far the cheapest solution, it also would have the advantage of being suitable for high pressure without any additional effort for reinforcement while the contribution to the radio purity levels is supposed to be much lower than for a system based on PMTs.

10.2 Use of quenchers

Operation in pure Xenon has been a requirement for most of the work with Micromegas within NEXT, in order to be able to detect the primary scintillation light for event fiducialization. The operation of proportional-mode charge readouts in pure noble gases is conventionally very problematic, as described before, and the demonstrated performance of Micromegas in pure Xe has been a remarkable result within the MPGD community. Nevertheless, it is clear that the potential of Micromegas, as any other charge readout, is fully realized with the use of a quencher gas added to the noble gas. As an example, benchmark results in Ar-isobutane mixtures (isobutane being a quencher of choice for Ar) provide systematically better performance than the one established in previous sections for pure Xe. Regarding energy resolution, factors of the order of 2 better are obtained. Other aspects are also favored in Ar-isobutane than in pure Xe, like achievable gain, ease of operation at high pressures, sensitivity to gas impurities, etc.

It is conceivable that the use of a suitable quencher for Xe could also provide significant advantages in one or more of these aspects:

- increasing the amount of primary charges via Penning effect, leading to improved energy resolutions.
- quenching the photon emission in the avalanche, leading to more stable amplification at high voltages, and higher achievable gains, and potentially also leading to better energy resolutions.
- increasing the drift velocity for a given reduced field value, potentially leading to the use of lower drift fields, simplifying high voltage solutions and improving energy resolution (by reducing the effect studied in [26]).
- improving transversal and longitudinal diffusion, leading to better topology information and eventually better background reduction.

Although some additives to Xe could be used while preserving the primary scintillation for t_0, more intriguing is the possibility of relaxing such strong requirement. This scenario would open a big range of

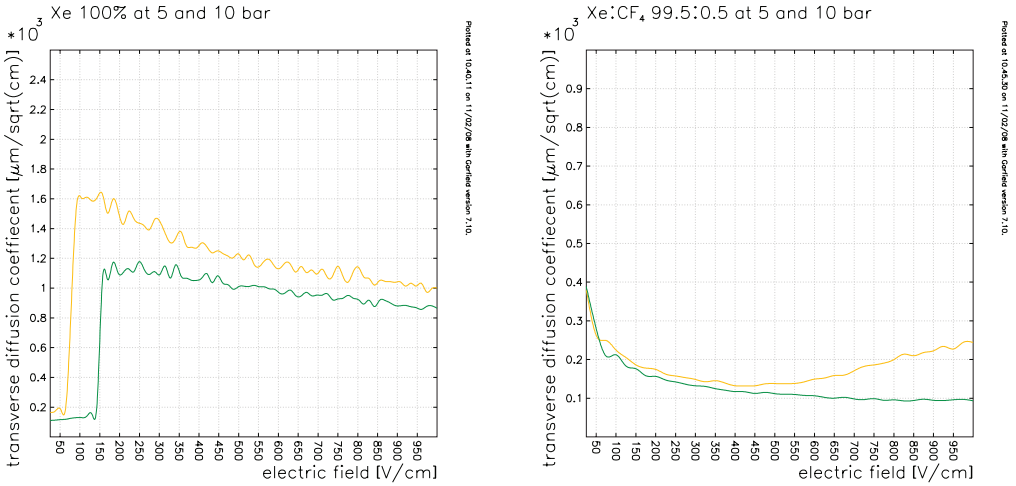

Figure 14: On the left, transversal diffusion of pure Xe at 5 (green line) and 10 (yellow line) bar versus the drift field. On the right the same for a mixture of Xe with 0.5% CF_4, showing an improvement of a factor $\sim$10

possible gas mixtures to optimize regarding the previous 4 points. The extent to which NEXT is feasible without primary scintillation is commented in the next two sections.

There is another possible motivation to explore the option of using additives to the Xe. Adding a low-Z species to the Xe will reduce the probability of the electron having bremsstrahlung emission. As commented in section 6, this emission is the cause of the major loss of efficiency of the topology cuts. Whether this emission can be substantially reduced in a practical mixture is to be seen. Studies are ongoing to quantify this effect.

Very recent unpublished data from Unizar group (see appendix A) suggest that the addition of a fraction of 20-40% of Ne to the Xe improves the gain in the Micromegas (tested in up to 5 bar pressure) and maybe also the energy resolution. In addition, molecules like TMA (trimethilamine) are known to form effective Penning mixtures with Xe. As advocated by D. Nygren[41], they might be used in small quantities while still preserving primary scintillation (and electroluminiscence). Old data with charge amplification in single wire proportional counter [42] exists with an impressive 7% FWHM energy resolution at 22 keV with additions of 5% or 10% of TMA to the Xe. A systematic study of this mixture at higher pressures with Micromegas is being carried out by the Unizar group. Preliminary results are very promising, showing indeed much larger gains than in pure Xe for the same voltages (as expected for a Penning mixture), larger maximum gain, and very stable operation. An energy resolution of 12% at 22 keV at 4 bar of Xe-2.5% TMA (see appendix A) has been already obtained (extrapolating to 1.2% FWHM at $Q_{\beta\beta}$. Better results seem achievable after optimization of the TMA fraction. It seems that 1% FWHM at $Q_{\beta\beta}$ is at hand of a Micromegas readout by using this kind of mixture. In addition, additives like CF_4 or CH_4 could be used to increase the drift velocity and the diffusion and to allow for operation at lower drift fields. As shown in figure 14, the addition of only 0.5% of CF_4 to the Xe reduces a factor of 10 the transversal diffusion even at the low drift fields needed to avoid the degradation of energy resolution studied in [26]. On the other hand, the use of Xe mixtures poses some technical questions, in particular regarding possible attachment from the additives and the issue of appropriate purification techniques. In any case, the phase space opened by the use of quenchers offers a large potential for improvement for NEXT that is worth exploring. Our baseline option leaves open the way to improvement via these

directions.

10.3 t_0 determination by ion detection at cathode

At every primary interaction a large number of positive ions (as many as electrons) are generated and they drift slowly towards the cathode. If these ions could be detected at their arrival at the cathode a precise information on t_0 or, equivalently, on the absolute z-position of the event could be obtained. Unfortunately, because ions do not trigger an avalanche, the charge signal induced in a given electrode structure (a wire plane or grid, for example) is rather small. Additional complication arises form the fact that the reading must be performed at an electrode at very high voltage. However, the amount of charge ($\sim 10^5$) involved should be sufficient for detection in ionization mode, and therefore the challenge seems to be of a technical nature. Recent work by the New Mexico University group [43], in the context of R&D for dark matter TPCs have demonstrated ion detection at the TPC cathode, with a sensitivity of only 900 ions (a signal 100 times weaker than ours). Some issues to consider are the fact the $\beta\beta$ ion cloud would arrive very much spread in time, so probably a special very slow readout electronics would be needed.

If this possibility is realized, our baseline detector could manage without PMT plane for t_0 measurement, thus avoiding the largest contributor to the background. Moreover, it would allow operation with any kind of quencher without worrying about preserving the primary scintillation, opening the way for the optimizations discussed in the previous subsection.

10.4 TPC without t_0

The measurement of t_0 has been a must for NEXT since the beginning. As largely proven by other rare event experiments, fiducialization is a very important issue allowing to reject a large fraction of events associated with edge effects. Now that first full background models for NEXT are available, we can evaluate to which extent this handle is important in NEXT, or whether the need for t_0 comes from a prejudice based on different assumptions and needs than the ones relevant to NEXT.

Fiducialization is powerfully utilized in liquid Xe TPCs, like EXO or XENON, but is also used to some extent in other rare event experiments (e.g. modern Ge bolometers). It is justified by the need of identifying and eliminating: 1) events that interact in the outer layer of sensitive volume (self-shielding); 2) events associated with surface contaminations (e.g. β emission) and 3) events associated with the presence of the boundary of the sensitive volume (incomplete charge collection).

In gaseous media like NEXT, self-shielding is not a relevant effect, so fiducialization affects only events associated to β emission from surface facing the sensitive volume or from incomplete charge collection (tracks starting in the gas and ending in the surface material or viceversa). According to the study presented in section 6, the fiducial cut allows a background rejection of a factor of 5 to 50 (depending on the type of contamination, and only for contaminations *in contact* to the sensitive volume, otherwise it is of order unity, see table 2). The non-availability of t_0 information would reduce the rejection power of the fiducial cut because only fiducialization in the $x-y$ plane would be possible. Naively assuming the effect to be proportional to the surface (in reality it will depend on the actual distribution of contaminations in the relevant surfaces), one could guess that the effect of the t_0 information on the rejection is of a factor of 2-17. Although important, this factor does not seem prohibitively high, especially if it allows for compensating measures like extra simplicity and radiopurity (avoiding PMTs) and more powerful topology cuts (due to the use of low diffusion gas). Moreover, a PMT-free cathode could be more easily optimized for ultra-low surface contaminations, and a good topological information could

allow to recognize events happening in contact with the readout, due to the exceptionally low diffusion that they would present. This opens a way to do a pseudo-fiducialization without t_0, which would add to the other measures.

In summary, although all these ideas need careful study and simulations, the considerations presented seem to point that a t_0-less operation of NEXT could be not only possible, but even competitive.

10.5 Electroluminiscence readout with APDs

The detector concept based on Micromegas charge readouts is certainly conservative and most suitable to achieve on a reasonable time scale a NEXT-100 detector, however as mentioned in section 9 it also contains risks. For many of them possible solutions are already considered in the previous subsection. Nevertheless, not all of these problems might be solved sufficiently to make this a competitive experiment on the long term but even for this case the presented detector concept allows a fall back solution by replacing the Micromegas readout by an EL-based readout. The possibility of using APDs to read the EL signal is particularly appealing among the possible EL-based configurations because both tracking and energy information are extracted from the APD readout, and therefore the philosophy of the original baseline MAGIC design is preserved, making it a natural possible evolution. This option is further developed in appendix C where an update of the status of R&D on APDs performed by IFAE group is also presented.

10.6 $\beta\beta$-tag through Čerenkov radiation

Recently I. Giomataris [44] has proposed the use of the Čerenkov emission that ∼2.5 MeV electrons would emit in high pressure Xe to tag them as background, and achieve a further, potentially very powerful, rejection factor. The density of the gas could in principle be adjusted so that the emission threshold would be below $Q_{\beta\beta}$ but above $\frac{1}{2}Q_{\beta\beta}$. In this way only background electrons would emit radiation, and not $\beta\beta$ electrons of typical energies $\sim \frac{1}{2}Q_{\beta\beta}$. The required density for this is between 10-20 bar. For higher densities $\beta\beta$ events would also emit Čerenkov radiation and the discrimination might be achieved by looking at the 2-cones emission versus the 1-cone one. In any case, the intensity of the emission is rather weak, so a large coverage of photosensors would be needed. An appropriate way to distinguish the Čerenkov light from the normal scintillation light is needed (maybe using different sensors with sensitivity to different wavelengths). In the scenario of a non-scintillating TPC of subsections 10.2,10.3 and 10.4, this problem is solved, and so this idea could be more naturally applied to one of these future stages of NEXT[44]. Although the idea is very appealing, it certainly needs detailed study and simulation in order to assess its feasibility and possible implementation in future NEXT stages.

11 Proposed staging strategy

Currently NEXT is actively performing R&D with small scale NEXT-0 and NEXT-1 prototypes (< 1 kg). The baseline design proposed here relies in part in the work performed in the NEXT-0 setups at Unizar and Coimbra, as well as the NEXT-1-MM prototype (see appendix A) at Unizar. Several of the aspects of the baseline design, as well as the ones commented as possible improvements of it, need further experimental verification in the ongoing NEXT-0-MM and NEXT-1-MM programs. Our proposal goes beyond defining a baseline design for NEXT-100, but rather a staging scenario in which the baseline design is tested in an intermediate detector (NEXT-10 project) and in parallel the NEXT-1 program is continued actively. The NEXT-100 design should then get enriched with the experimental feedback from

the NEXT-1 and NEXT-10 experiences, in order to minimize risks and assure the selection of the best option.

Although we acknowledge the merit of advancing fast towards a design for NEXT-100, we need to balance it with the risks of jumping to a 100 kg detector without a proper demonstrative experience at an intermediate scale and, in some senses, not even at a small scale. In our view, the compromise solution is to exploit synergies and complementarities between the NEXT-1 and NEXT-10 experiences. A NEXT-10 intermediate detector, built upon a conservative baseline design, is needed to test and demonstrate the background solutions proposed. The radiopurity, shielding and topology cuts, and in general the NEXT background model assumptions, are crucial points for NEXT success as discussed in section 6. NEXT-10 would demonstrate it (or would pinpoint the possible weaknesses of it, allowing for correction at NEXT-100). NEXT-100 design would be built upon a improved design taking into account feedback from NEXT-1 and NEXT-10 programs. Alternatively, it could be considered to build a first version of NEXT-100 (and therefore quicker) based on a relatively conservative design close to NEXT-10 and contemplate possible enhanced stages of NEXT-100 after complete feedback from NEXT-10 and NEXT-1 becomes available. In any case, flexibility in the starting point and connection with R&D work are two main points of this proposal.

12 Summary

We have presented a baseline conceptual design for NEXT-100 based on a Micromegas charge readout as the main element providing topology and energy information of the event. Measurement of the primary scintillation is achieved by means of a sparse PMT array located behind the cathode. A competitive performance could be obtained by this detector, under the assumption of an energy resolution of 2.5% FWHM at $Q_{\beta\beta}$ at 8 bar of pure Xe, as indicated by current results in low scale prototypes, and the construction of the detector out of very radiopure materials. A realistic background model has been built using radiopurity levels of all the materials entering the inner detector components. The merits of this proposal relies on its cost-effectiveness, its relative simplicity, the conservative use of materials regarding their radiopurity, and the possibility of implementing future improvements.

Improvement of the energy resolution, quality of the topology information, and background levels seem available through a series of enhancements beyond this baseline design. As an example, operation in a suitable Xe mixture could potentially improve Micromegas operation, its energy resolution and the background rejection power through better topology cuts. Combined with an alternative t_0 measurement that could avoid the PMT plane (as most probably the additives to the Xe would quench the primary scintillation), it would lead to further radiopurity of the detector. These options need close monitoring by NEXT as they may constitute the basis of future NEXT stages, or of mitigation plans after possible unforeseen shortcomings of the baseline design.

We have proposed a staging scenario for NEXT in which the baseline option is tested on a intermediate detector NEXT-10, while continuing the R&D with the NEXT-0 and NEXT-1 setups. NEXT-10 would also test the background assumptions and solutions for NEXT-100. Eventually NEXT-100 would be defined with a more or less conservative profile, but allowing for a subsequent stage with one or more of the enhancements envisaged once they become established by the R&D.

Appendices

A Summary of results with microbulk readouts

NEXT-0-MM is the first small prototype[6] built in order to test microbulk planes in high pressure. It is a 2 litre chamber made of Stainless Steel, with a diameter of approx. 14 cm and a drift region of 6 cm. The vessel has been tested to hold pressures of up to 12 bar. With the help of resistors fitted at its exterior, the vessel can be heated up to 110 °C. A field cage consisting in 6 copper rings held together with three columns made of PEEK and interconnected by resistors. The structure is topped by a copper disk as a cathode. A hole is made in the cathode to accommodate the sources used in the tests (figure 15).

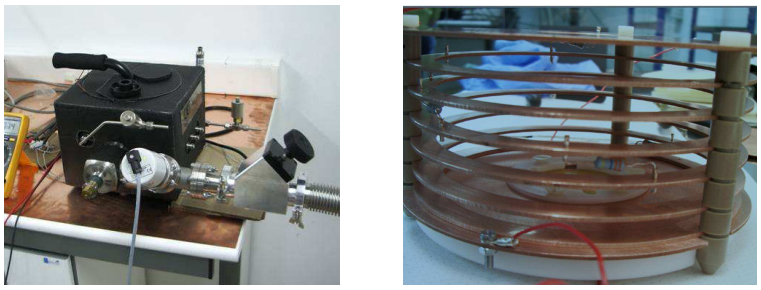

Figure 15: On the left, a photo of NEXT-0-MM. The vessel is covered with an insulator layer (black). On the right, the field cage of NEXT-0-MM: six copper rings interconnected via resistors, held in place by three PEEK bar and a copper disk as a cathode on top.

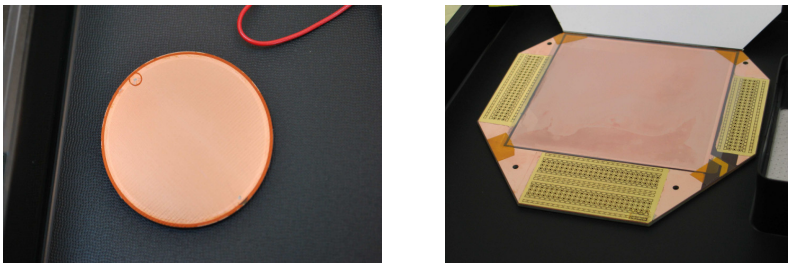

Figure 16: On the left, the first generation of microbulk Micromegas used. They have a diameter of 35 mm and an amplification gap of 50 μm. On the right, the first large microbulk built, with a segmented anode. It has an active area of $10\times10\,\mathrm{cm}^2$ divided into 144 pixels.

Two types of microbulk Micromegas have been used for the tests in NEXT-0-MM: circular readouts with an amplification gap of 50 μm and 35 mm diameter whose anode was not segmented and a bigger one, with an active area of $10\times10\,\mathrm{cm}^2$ (figure 16). The latter has a pixelized anode with a total of 144 pixels and at the time was the largest Micromegas built with the microbulk technique. During the tests both signals of the anode and of the mesh are recorded.

[6] Although the first results with microbulk readouts at high pressure were obtained at the HELLAZ setup in Saclay [8]

At the first phase of the measurements, the response of the detectors in different mixtures of Ar-Isobutane was studied, with the concentration of Isobutane in the mixture varying from 0.1% to 5%. The pressure inside the vessel was raised up to 10 bar and the tests were done with the alphas coming from an ^{241}Am source. The best energy resolution achieved in that configuration was 0.7% (FWHM) for the 5.5 MeV of the alphas coming from an source, at 4.75 bar in Ar-2%iCH_4 gas mixture.

At a later stage, measurements were performed introducing pure Xenon in the chamber increasing the pressure up to 5 bar. In the range between 2 and 5 bar energy resolutions around 3% (FWHM) for the 5.5 MeV alphas of the ^{241}Am source were obtained [9], the best one being 2.5% for the 4 bar case.Using a selection of events based on risetime the aforementioned values improve to ∼2% (FWHM) (the best value at 1.8% FWHM for the 4 bar case). The system was working mainly in a closed mode, meaning that the gas was introduced and then the vessel sealed. However, at times the gas was recirculated in the system and purified while passing through a filter. In all the cases, the limitation in the measurements was the gas quality; the energy resolution measurements started to be clearly affected by attachment.

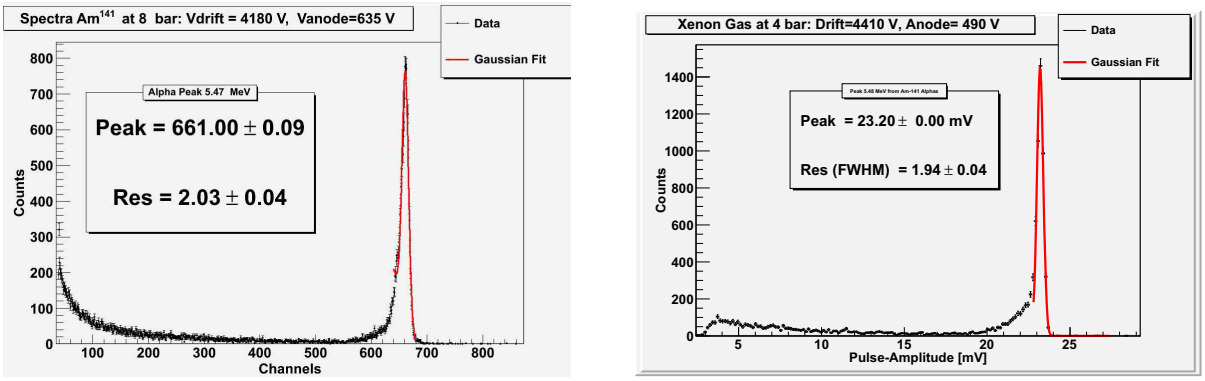

Figure 17: Energy spectra of the ^{241}Am 5.5 MeV alpha peak measured on the left at 8 bar of pure Argon, showing an energy resolution of 2.03% FWHM, and on the right measured at 4 bar of pure Xenon, showing an energy resolution of 1.94% FWHM.

The second campaign of measurements was focused on pure Ar and pure Xe gases. The quality of the gas was improved after long pumping periods but as well after prolonged bake-out periods in vacuum and circulating warm Nitrogen gas through the system. Figure 17 shows the best results achieved in each case, for the 5.5 MeV α of the ^{241}Am, namely 2.03% (FWHM) at 8 bar of Ar and 1.94% (FWHM) at 4 bar of Xe. Under these conditions the effect of attachment in the gas started to be evident only in higher pressures, allowing thus data-taking up to 8 bar in pure Ar and pure Xenon. At 8 bar of Xe, the attachment effect was already apparent and therefore the resolution achieved of 4.8% (FWHM) at 5.5 MeV was not as good.

By this time, when the pixelized microbulk detector was used, part of the pixels were read with a reduced version of the T2K electronics, allowing the 3D reconstruction of the tracks gathered. Figure 18 shows an ^{241}Am alpha track in pure Ar at 1.23 bar, as recorded in the two-dimensional plane, and its reconstruction.

Measurements with γ in pure Xe Flipping the ^{241}Am source upside down, the α emitted from the deposition remain blocked. Nevertheless, the source emits a γ line at 59.54 keV, which served to probe the lower energy region. Measurements were done at 1, 2 and 3.5 bar. These first measurements at high

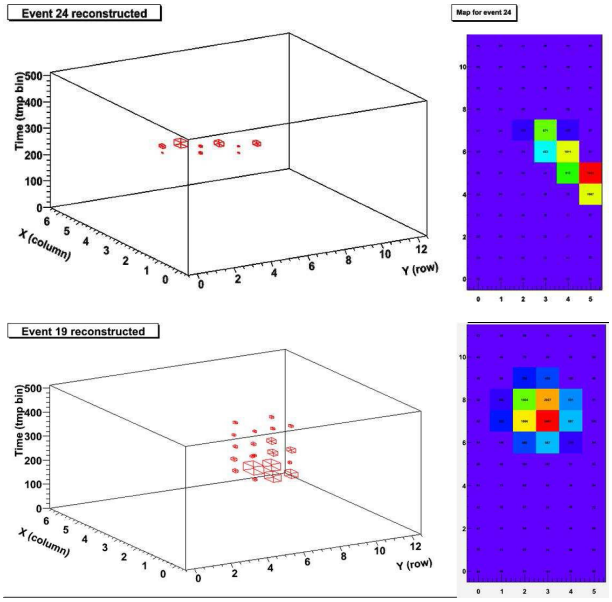

Figure 18: Projections of alpha tracks obtained with the ^{241}Am source in NEXT-0-MM in $\sim$1 bar of Ar-2%iCH$_4$ (up) and in pure Ar (down): 2D mapping of the events (right), as acquired with a reduced version of the T2K electronics, and their 3D reconstruction (left).

pressure, yield an energy resolution of 7.8% at 2 bar and 9.3% (FWHM) for the 60 keV γ of the ^{241}Am at 3.5 bar (figure 19). If extrapolated to the $Q_{\beta\beta}$ value of Xe (2458 keV), they would correspond to 1.2% and 1.45% (FWHM) respectively.

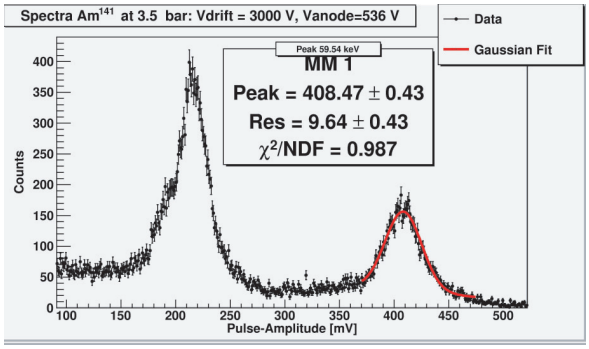

Figure 19: Spectrum of 59.54 keV γ in pure Xenon at 3.5 bar with an energy resolution of 9.6% (FWHM). The spectrum is acquired with an ^{241}Am source from which the alphas were blocked. The peak on the left is composed mainly of escape peaks from the 60 keV α, due to the fluorescence of Xe at 30 and 33 keV and partly of the 26 keV γ line of ^{241}Am.

Interesting results in high pressures were obtained by Coimbra and Saclay with a smaller setup [10], where the drift length was 7 mm. The measurements on the energy resolution of the charge and the scintillation channel, were performed in pressures of Xe varied from 1 to 10 bar. The results obtained show a good operation in high pressures with high charge gain, above 10^2 for all pressures, as plotted in the left part of figure 20. However the energy resolution for the x-rays of 22 keV of a ^{109} Cd source shows an increase from 13% at 1 bar to 31% at 10 bar (right-hand part of figure 20). These results could be improved in an optimized setup with a selected Micromegas detector.

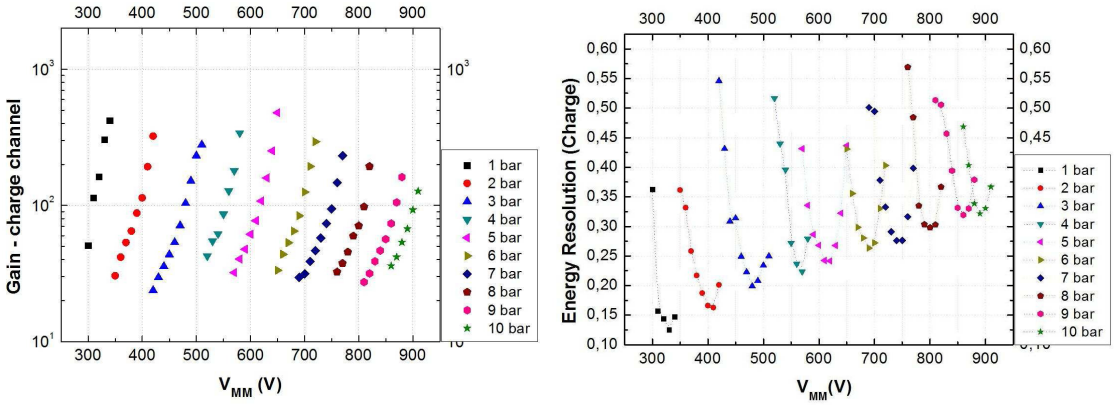

Figure 20: Measurements with a microbulk Micromegas in the Coimbra setup using 22 keV γ in Xe pressures of 1 to 10 bar. On the left, the charge gain of the microbulk as a function of the Micromegas voltage, showing high enough gains for measurements in high pressures. On the right, the energy resolution as a function of the Micromegas voltage. A worsening of the energy resolution is noted following the increase of pressure of Xe. Plots taken from [10].

Tests with Xe-Ne mixtures Another series of measurements were taken, with mixtures of Xenon with different concentrations of Neon at pressures up to 5 bar. The source employed was the ^{241}Am which emits alphas of 5.5 MeV. The main conclusion of these measurements is that there was a clear increase in the gain of the Micromegas in the Ne mixtures with respect to the one in pure Xe. Regarding the energy resolution measurements, similar values were obtained as in the case of pure Xe, as presented in figure 21, although for a wider range of amplificatio fields. Due to a non-optimal performance of the readout used in these measurements, it is not excluded that better energy resolutions could be achieved with this mixture.

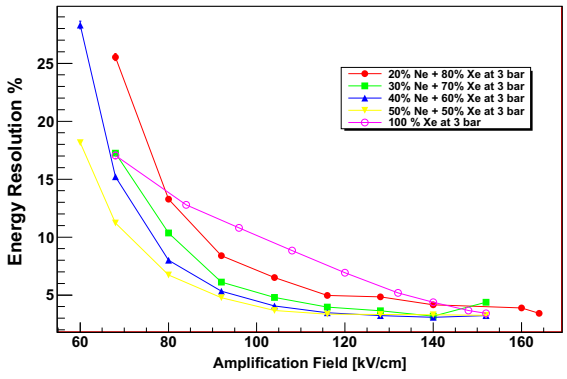

Figure 21: Results on energy resolution measurements with the different Ne-Xe mixtures. No significant improvements are observed with respect to the results obtained in pure Xe at higher fields.

Tests with Xe-TMA mixtures TMA is known to form a Penning mixture with Xe. Old results [42] performed in single wire proportional counters showed gains up to 10^4 (and much higher than other mixtures for the same amplification voltage), and energy resolutions down to 7% FWHM at 22 keV for a TMA fraction of 10%. A systematic study of this mixture with Micromegas and high pressures is ongoing by the Unizar group. First measurements have been done with gas mixtures of Xe and small percentages of TMA (Trimethylamine). As expected, the gain of the Micromegas increases by at least one order of magnitude with respect to the yield in pure Xe. Very preliminary results of a measurement with a Xe-2.4%TMA mixture at 4 bar show an energy resolution of 12.6% (FWHM) for the 22 keV photons of a ^{109}Cd source (which would translate into a 1.2% (FWHM) at the $Q_{\beta\beta}$ of Xe). Better results are expected after the optimization of the TMA fraction in the mixture.

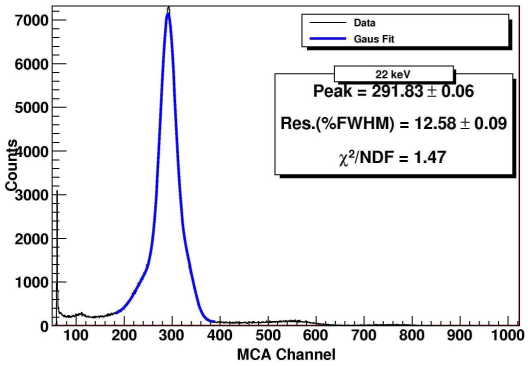

Figure 22: Preliminary energy spectrum recorded with a ^{109}Cd source in a Xe-2.4%TMA gas mixture at 4 bar. The energy resolution achieved is 12.6% (FWHM) at 22 keV. It should be mentioned that the fit contains the four peaks present (22 keV, 25 keV and their escape peaks at ∼16 keV and 19 keV).

B Status of NEXT-1-MM prototype

NEXT-I μM is a prototype mainly designed to test Micromegas detectors inside high pressure Xe atmosphere. With this purpose an 80 litres volume ($\sim$ 40 cm in diameter, 53 cm drift-length) Stainless Steel vessel was manufactured covering the required specifications to work up to 10 bar (figure 23).

The main premises to design this prototype were the capability to reach pressure values around 10 bar and vacuum and outgassing levels low enough to assure the purity of the gas placed inside the vessel. Other important issues for the final setup of the experiment, like radiopurity, were not considered for the development of the prototype. These requirements implied a special selection of all the materials placed inside the vessel, trying to use these with an outgassing rate as low as possible (i.e. PEEK, delrin or cirlex).

The main objective of the operation of this prototype is to test *microbulk Micromegas* detectors in high pressure Xe atmosphere, trying to simulate the expected environmental features of the NEXT-100 experiment regarding gas and pressure. Complementary to this, the operation of this prototype allows to test different solutions and techniques applicable to the final phase of the experiment: feedthroughs, the field cage or bake-out system are some of the issues that could be checked.

When NEXT-I μM was installed in the Zaragoza laboratory, only certifications of vacuum and pressure were given by the manufacturer. In order to check these certifications, vacuum, pressure and out-

Figure 23: A photo of the NEXT-1-MM prototype and its supporting structure.

gassing test were developed before to equip the vessel. In addition, a bake-out system was installed allowing to increase the temperature of the vessel up to 200 °C.

Promising results were obtained from these preliminary tests. TRINOS (manufacturer) certified that a pressure of 5.6×10^{-6} mbar could be reachable after 22 hours of pumping. This result was checked since a pressure of 7.8×10^{-7} mbar was reached after 95 hours pumping cycle and equivalent values were also reached after the opening and *re-closing* of the vessel. After the installation of the mentioned bake-out system[7] and the realization of a bake-out cycle of ∼100 hours heating the system up to 180 °C, a pressure of 8.4×10^{-7} mbar was reached, After the improvement of the system, mainly after the installation of metal O-rings and gaskets, and new bake-out cycles, pressure level reached went down to 6.3×10^{-7} mbar.

As mentioned, a pressure test was done putting inside the vessel 11 bar of Ar gas.It was checked that no variations of the pressure, except the related to temperature oscillations, were observed along more than 10 days.

In parallel to the different vacuum and pressure tests done, systematic outgassing measurements were performed, especially after the installation of any new component inside the vessel. After some of these cycles and materials added, it was observed, that the outgassing rate decreases during the time even if some new elements were placed inside the vessel. This leads to think that bake-out cycles *clean* the different materials and they remain clean even if the the vessel is opened. Numerically, the main conclusion is that outgassing rate remains below 10^{-5} mbar×l/s even when all the required elements for the detection are placed inside the vessel (detector, field-cage and feedthroughs mainly). It is expected to improve this value making systematic bake-out cycles when the vessel will not be taking data, based on the improvement of the outgassing rate observed in the previous cycles.

The first measurements were carried out using a bulk Micromegas detector (left part of figure 24). This detector was specifically designed to be placed in NEXT-I μM, having a sensitive area of 30 cm diameter. This area is covered by 1152 pixels of ∼0.9 cm side which allow to register not only the energy of the event, but also the track.

In a first test, a ^{222}Rn source was diffused inside the vessel together to ∼1 bar of Ar-2%iCH$_4$. Using this source, 3 alpha emissions of 5.5, 6.0 and 7.7 MeV could be detected. The pixels of the detector were short-circuited and grounded while the signal was obtained by the mesh at the operation voltage. The

[7]For more details of the system see for example H. Gómez talk at the Coimbra NEXT Coll. Meeting (October 2009).

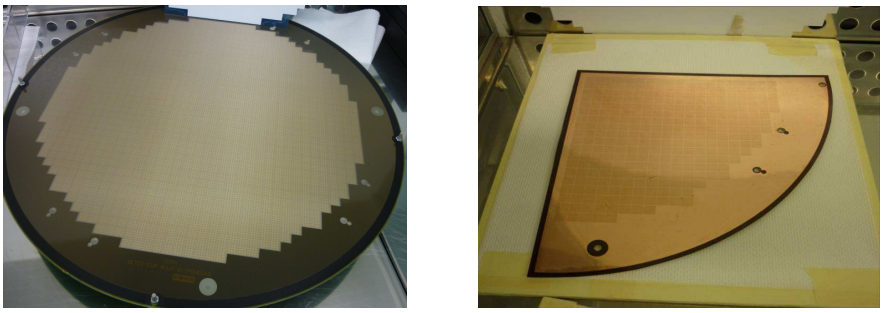

Figure 24: Photos of the Micromegas readouts manufactured to equip NEXT-1-MM. On the left the bulk Micromegas detector installed in the NEXT-1-MM; it has a diameter of ∼30 cm and its anode is segmented to ∼1200 pixels. On the right, the new microbulk Micromegas recently constructed. It is one of the four sectors to be installed in order to cover the sensitive surface of NEXT-1-MM.

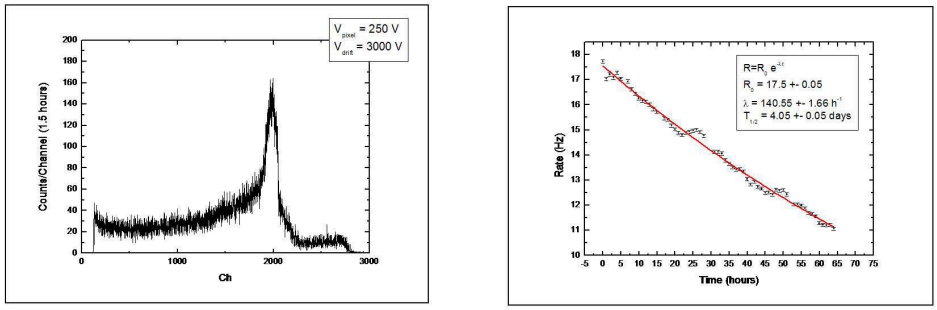

Figure 25: On the left, energy spectrum of the bulk Micromegas placed inside NEXT-I μM with ∼1 bar of Ar-2%iCH$_4$ and ^{222}Rn source diffused. On the right, the rate evolution over time, showing the ^{222}Rn decay half-life.

left part of figure 25 shows a spectrum with three alpha peaks. This is corroborated by the detection rate evolution, which fits the ^{222}Rn decay half life as it can be seen on the right part of figure 25. This first test proved the good running of the bulk detector and the good quality of the gas placed inside the prototype.

Using the T2K DAQ, with the same source in the gas, we registered not only the mesh signal, but also the pixel signals[8]. These first tests have as main goal the tuning of the DAQ system to the signal features expected in NEXT-I μM and the development of the analysis tools to obtain particle tracks from pixels signals. In any case, the first tests were successful and several events were recorded, allowing the 2-D reconstruction of the track and a 3-D distribution of the energy deposits as seen in figure 26.

As the main goal of the prototype is to test microbulk Micromegas, which are expected to obtain better energy resolution values, sector detectors with the same pixel configuration were developed at CERN to cover the 30 cm diameter area (right-hand part of figure 24. The first two sectors have been tested in a test chamber using ∼1 bar of Ar-2%iCH$_4$ and an ^{241}Am source (providing a 5.5 MeV alpha emission). Preliminary tests showed a good behaviour of the detectors, being ready to be installed at NEXT-I μM to take data at different configurations (gas mixture and pressure, drift and amplification

[8]For more details of this DAQ see for example H. Gómez talk at the Santiago NEXT Coll. Meeting (April 2010).

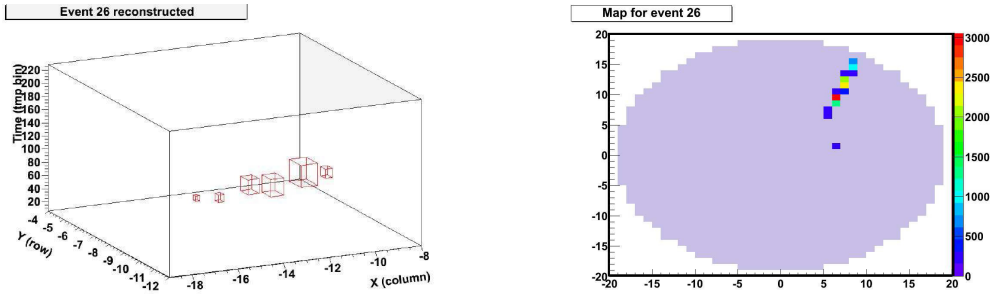

Figure 26: Example of an event's 3D distribution of the energy deposit (left) and 2D track reconstruction (right). The shaded area indicates the active area of the bulk Micromegas.

field) recording both event energy from mesh and track from pixels.

In conclusion, NEXT-I μM is the medium size prototype used to test Micromegas solution for data taking in NEXT-100. The prototype allows the testing of the detectors in a 35 cm-length field cage with gas pressures up to 10 bar. There are two sources of information from the detector, the mesh signal for the event energy but also the track from the pixels signals, using for that an AFTER based DAQ. After the first tests that assured the necessary vacuum, pressure and outgassing conditions to work with the detectors, $\sim$30 cm-diameter active area bulk Micromegas were successfully tested. Preliminary tests to cover the same area with microbluk Micromegas were also performed in a test chamber, being imminent the installation in NEXT-I μM for commissioning.

C Summary of results with APDs

The disadvantage of a charge readout is that the exponential amplification introduces fluctuations in the measurement limiting the achievable energy resolution. In an electroluminescent (EL) readout this charge amplification process is replaced by a light amplification. Primary electrons drift to a region which is concluded by two wire meshes. Between the two meshes a voltage is applied such that the electrons excite the gas, normally pure noble gases as xenon or argon, without ionizing it. In the de-excitation of the atoms, photons in the VUV region are emitted isotropically. Since this is a linear process, the gain fluctuations introduced are smaller and therefore the achievable energy resolution is significantly better. The amount of photons produced depends on the applied voltage difference, the distance between the two meshes and also on the operation pressure. It turns out that the performance improves with increasing the pressure in contrast to a charge readout. In [45] a detailed description of the process for xenon can be found.

The use of APDs for the readout of EL chambers was already studied intensively by a research group at the University of Coimbra [46]. Their results (left part of figure 27) with a single APD readout indicate that an excellent energy resolution of less than 5% can be achieved at 22 keV for pressures between 4 to 6 bar. The authors believe that the rise for higher pressures is caused by experimental effects (micro sparks) in their setup. If this result could be scaled with $1/\sqrt{E}$ to the $Q_{\beta\beta}$ of xenon (2.46 MeV), an energy resolution of significantly better than 1% FWHM at 2.46 MeV would be possible. They also compared directly the performance of reading out the chamber with an APD to the one achieved with a PMT [47]. The result is shown in the right-hand part of figure 27. As one can see the energy resolutions with these two kind of sensors are very similar under the same experimental conditions.

In the following the results obtained with a 5 APD readout are summarized, followed by a set of

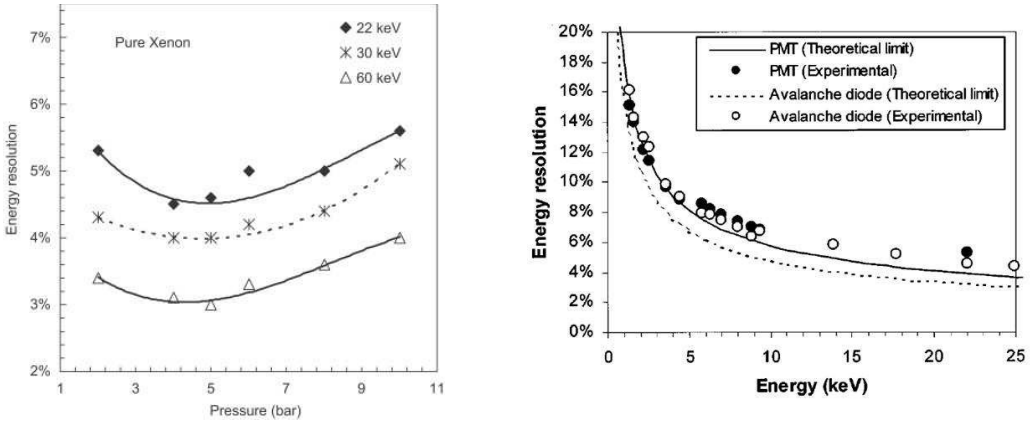

Figure 27: On the left, energy resolution and gain as function of the pressure for three different energies [46]. On the right, direct comparison for the achieved energy resolution with one PMT and one APD [47].

simulations showing a very good understanding of the physics and which will be the basis to extrapolate to larger readout areas in the future. This section will be concluded by an argumentation why a direct step to a 100 kg detector with this readout technology is not preferable.

C.1 Experimental results

Experimental tests were performed with a readout consisting out of 5 APDs (S8664-55-SPL) from Hamamatsu. These are standard APDs without the protection window which normally absorbs VUV photons. The APDs have a size of 5x5 mm^2. A 10x10 mm^2 version is also available. These APDs are directly sensitive to the EL light of xenon (172 nm) with a quantum efficiency of about 80% according to the data sheet. Measurements performed together with the research group at the University of Coimbra gave a result of 70±16%. During the tests the same bias voltage is applied to all 5 APDs, while the signal from each is read out independently. This powering scheme introduces a high correlation between the noise of the APDs. Proper treatment of the pedestal correlation might help improve further the energy resolution and it is under investigation.

For the signal creation a ^{109}Cd source was used which emits mainly X-rays at 22 keV and 25 keV. The source is located on top of the central APD. The data taking is triggered by a threshold requirement on the energy deposition in the central APD while no requirements are applied to the outer APDs. After 1000 data events, 10 events with random trigger are taken to determine the pedestal and noise continuously during the data taking. The gain and energy resolution were measured for a wide range of parameters as drift field, EL field, APD voltages at various pressures between 1 and 1.65 bar.

The energy deposition in the APD array is measured by adjusting the photon profile obtained from the MC. The fit adjusts simultaneously the coordinates in the APD readout plane, the integrated energy and a parameter that allows to scale the photon profile width. This parameter is a measurement of the drift distance as it can be seen in figure 28 where this scale factor is plotted as a function of the true drift coordinate position. The reconstructed energy as function of the photon distribution scale factor is shown for data and MC in figure 29. The best energy resolution obtained with this method is (8.2±0.1)% FWHM.

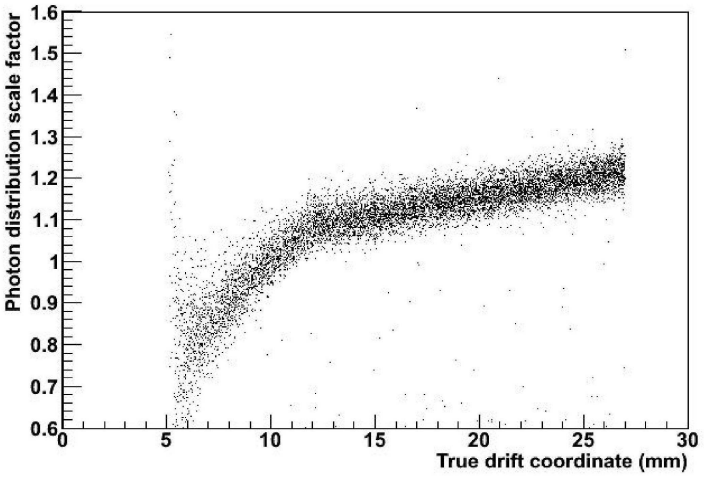

Figure 28: Photon scale factor spatial dispersion as function of the drift coordinate from MC simulations. The region between 5 and 12 mm corresponds to the conversions in the electroluminescence gap.

This is not the optimal method to reconstruct the energy, in the future the z coordinate will be measured from the event t_0 given the exact position in the drift volume. Since we do not have a measurement of the event time, the best energy resolution is obtained by fixing the scale in an effective position z and adjusting the energy and the photon conversion coordinates in the APD plane. The best result for the energy resolution with this method is (7.4±0.1)% FWHM as shown in figure 30. The data are restricted to an active area of ±5 mm around the center of the chamber. An inter-calibration between the APDs is applied to the data for this result. The peak of 25 keV is clearly visible. The additional peak which can be found at 8 keV, see figure 31 is caused by X-ray fluorescence at the copper of the cathode. This peak has an energy resolution of 15.7% which is worse than expected when scaled with $\sqrt{E}$, we assume due to a higher noise contribution. A low threshold of about 2 keV can be achieved with such a readout at 1.65 bar. Further improvement can be expected for higher pressures as shown in the left part of figure 27. However, already a simple scaling this energy resolution to 2.5 MeV already confirms the expectation for an energy resolution far better than 1% at the Q value of Xenon. The potential performance for larger APD and higher pressures is discussed in the following section.

The absolute calibration is done with respect to the main Cd peak (22.2 keV). After the fit, we obtained 22.21±0.012 keV for this peak. The value of the Cu peak is obtained at 8.19±0.03 while it is expected at 8.15 keV, this is a linearity of 0.49±0.36% at the Cu peak. The value is significant because the Cu fluorescence peak is close to the detector threshold where noise handling is critical for the linearity performance. The detector threshold can also be estimated from the spectrum plot to be around 2.5 keV. This value is expected to improve with the pressure. For example at 10 bar, the number of photons per electron is around 2200 (compared to 510 at 1.65 bar) giving an estimated threshold of 0.6 keV.

C.2 Simulations

A fast Monte Carlo simulation was used to better understand the relevance of the different factors limiting the final energy resolution. The geometry of the detector is fully implemented. We consider point-like energy depositions produced by conversions of ^{109}Cd x-rays in the sensitive volume (drift and EL regions). Each conversion produces 45.45 drift electrons per deposited keV on average, with a Fano factor

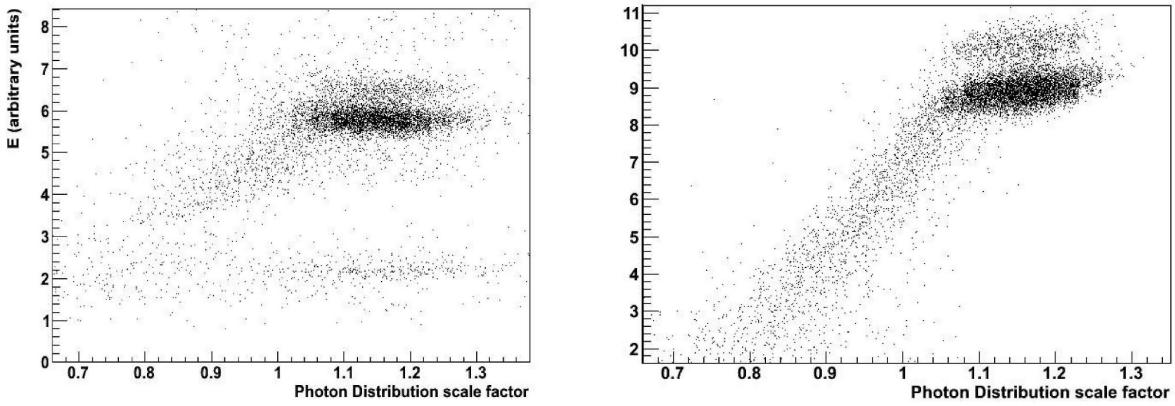

Figure 29: Reconstructed energy as function of the photon scale factor spatial dispersion for the data (left) and MC(right). The electroluminescence region is clearly seen in both figures.

of 0.15. For conversions within the drift volume, the transversal diffusion is simulated by the convolution with a Gaussian distribution of $\sigma = \eta\sqrt{z}$ mm, where $\eta = 0.553\sqrt{\mathrm{mm}}$ is the diffusion coefficient for the experimental conditions and z is the drift distance in mm. Drift electrons produce photons isotropically within the EL region. The average number of photons produced by an electron traversing the full EL region is 510 (with Poissonian fluctuations). Proportionally less photons are produced for shorter traversed EL distances (for x-ray conversions in the EL region). Photons arriving to the APD plane are recorded. The non-transparency of the EL meshes to both the primary x-rays and secondary EL photons is taken into account. The average profile of photons arriving to the APD plane as a function of the coordinate z of the initial conversion is used in the energy reconstruction, as described in the previous section. The number of photons detected by the different sensors are computed out of these profiles by masking them using the APD grid geometrical configuration, and applying a quantum efficiency of 80%.

The noise is simulated assuming a 70% correlation among all the APDs and a total noise level of 340 photons. These numbers are obtained from the combined fit of the Cu and Cd peak in the data and it is comparable with the numbers obtained from the simple sum of the APD pedestals. The noise for the 10x10 mm^2 APDs are rescaled pessimistically with the area of the APD. The results are shown in Table C.2 for 5 mm APD and Table C.2 for 10 mm APD. The agreement between data and Monte Carlo is remarkable and gives some confidence on the extrapolation to larger gas pressures. The results show that the resolution at 10 bar should be better than or the order of 4% FWHM for 22 keV (i.e. 0.37% FWHM at 2.5 MeV). This result also shows that the actual setup at the IFAE is limited by the APD and electronic noise. The 10x10 mm^2 APD show worse results to the ones with 5x5 mm^2, the main reason for that is the pitch that is almost 50% worse. In fact, the fraction of photons in the outer 4 APDs compared to the central one is 0.52 while this number is reduced to 0.37 for 10 mm APD. This value depends strongly on the transverse diffusion and it will be less relevant for longer drift distances.

C.3 Discussion

The preliminary studies show a great potential for EL readout combining tracking and energy measurements in a single plane. Although the data were taken with a small readout of only 5 APDs, extrapolations to large area readouts can be based on this data set since the energy deposition per voxel in the final de-

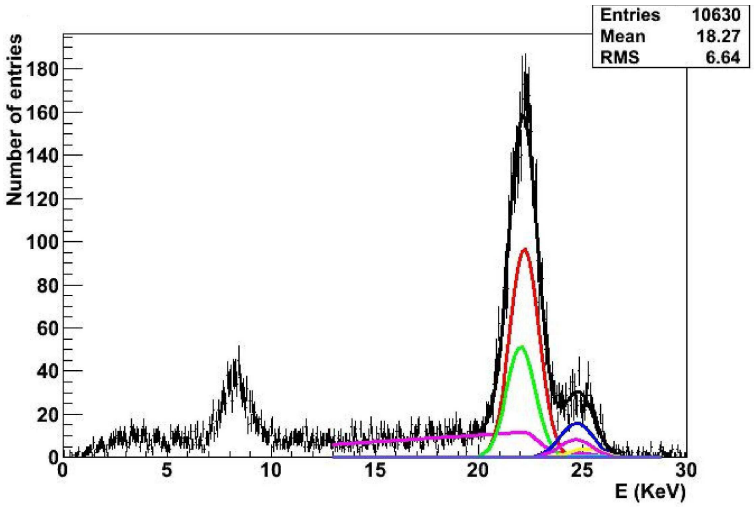

Figure 30: The best result achieved for the energy resolution was: (7.7±0.1)% FWHM for the 22 keV line. The settings for this run were: drift field: 300 V/cm/bar, EL field: 4 kV/cm/bar, APD bias voltage: 410 V, pressure 1.65 bar. The different colours show the relative contributions of the different ^{109}Cd x-ray peaks and the pink line starting at 13 keV describes the conversions in the EL region.

γ/e-	Resolution scale free fit (no noise)	Resolution fixed scale fit (no noise)
510	8.2 % (4.1 %)	7.2% (3.9%)
2200	3.6 % (3.2 %)	3.7% (3.2%)
Data	7.9 %	7.4%

Table 8: Energy resolutions obtained with two MC models for APD areas of 5x5 mm^2 and pitch of 10.3 mm. Data results are added for comparison.

tector will not differ too much from the one obtained in the given measurement serie. This method also avoids the difficulties of shifting the EL light and the non uniformities produced during the light transport from the anode to the cathode.

The cost of such a readout is certainly a drawback. In the mass production of APDs of 5x5 mm^2 cost about 250 Euro/piece and 10x10 mm^2 about 500 Euro/piece considering between 3500 (2x2 cm^2 pixel size) and 13500 APDs (1x1 cm^2 pixel size). Also the radiopurity contribution will require further investigation. The contribution of the silicon itself is certainly negligible but further studies are needed for the contribution of the packaging in which the APDs are delivered. Depending on the results of this study a time consuming optimization of the packaging in collaboration with Hamamatsu might be required, taking into account the small difference between the Bi peak position and the $Q_{\beta\beta}$ value of xenon. One also has to consider that a large TPC with EL readout was never built in contrast to a charge readout TPC. This introduces significant higher risks for the construction of an EL detector and requires many additional studies which do not fit with the given time scale for NEXT. For example, to our knowledge, never before was an EL mesh of a diameter larger than 1 m built. The design and optimization of such an EL mesh certainly can take a long time. Another delicate design parameter is the uniformity of the readout plane, both for calibration and surface coverage. The best option is a uniform

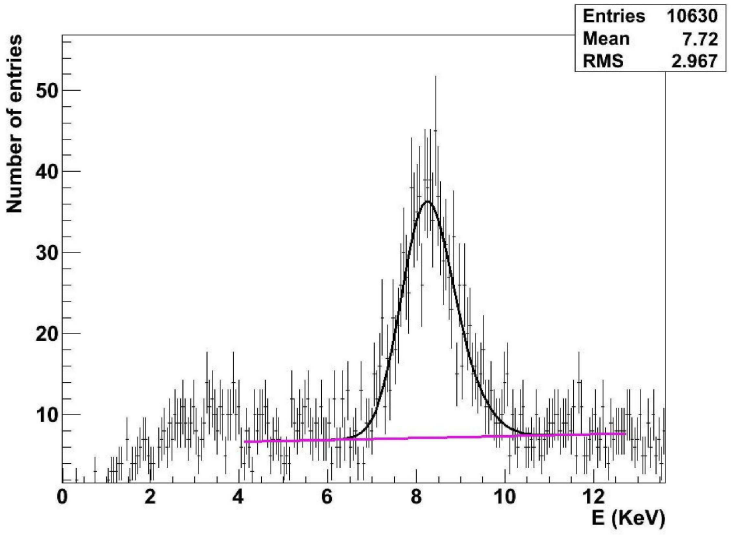

Figure 31: The best result achieved for the energy resolution was: (15.5±0.1)% FWHM for the 8.15 keV line. The settings for this run were: drift field: 300 V/cm/bar, EL field: 4 kV/cm/bar, APD bias voltage: 410 V, pressure 1.65 bar.

γ/e-	Resolution scale free fit (no noise)	Resolution fixed scale fit (no noise)
510	11.9 % (4.2 %)	8.7% (3.7%)
2200	4.5 % (3.8 %)	4.4% (3.2%)

Table 9: Energy resolutions obtained with two MC models for APD's areas of 10x10 mm^2 and pitch 15.3 mm.

readout plane (like the MM) even if the energy resolution is slightly worse, some new technologies like photon-counters allows for this uniform readout plane and it should be explored also because of its reduce cost with respect to solid state devices. Therefore the most success promising approach is to start with a charge readout while the EL readout is developed further with chambers of size of NEXT-1 and later followed by a chamber of size NEXT-10.

References

[1] J. I. Collar and Y. Giomataris. Possible low-background applications of MICROMEGAS detector technology. *Nucl. Instrum. Meth.*, A471:254–259, 2000.

[2] I. G. Irastorza. MICROMEGAS for rare event detection. *Proceedings of Identification of dark matter 2006. Rhodes, Greece, 11 - 16 September 2006*, pages 382–387.

[3] S. Ahlen et al. The case for a directional dark matter detector and the status of current experimental efforts. *Int. J. Mod. Phys.*, A25:1–51, 2010.

[4] S. Aune et al. New Micromegas detectors in the CAST experiment. *Nucl. Instrum. Meth.*, A604:15–19, 2009.

[5] S. Andriamonje et al. Development and performance of Microbulk Micromegas detectors. *JINST*, 5:P02001, 2010.

[6] T. Dafni et al. New Micromegas for axion searches in CAST. *Nucl. Instrum. Meth.*, A628:172–176, 2011.

[7] J. Galan et al. Micromegas detectors in the CAST experiment. *JINST*, 5:P01009, 2010.

[8] T. Dafni et al. Energy resolution of alpha particles in a microbulk Micromegas detector at high pressure Argon and Xenon mixtures. *Nucl. Instrum. Meth.*, A608:259–266, 2009.

[9] S. Cebrian et al. Micromegas readouts for double beta decay searches. *JCAP*, 1010:010, 2010.

[10] C. Balan et al. Micromegas operation in high pressure xenon: charge and scintillation readout. *JINST*, 6:P02006, 2011.

[11] S. Cebrian et al. Radiopurity of Micromegas readout planes. *Astropart. Phys.*, 34:354–359, 2011.

[12] G. Luzón et al. Background characterization of the new canfranc underground laboratory. *Proceedings of the 6th International Workshop on the Identification of Dark Matter (IDM2006)*, pages p. 514–519, 2007.

[13] NEXT shielding working group. NEXT shielding report.

[14] GERDA Experiment. Progress Report to the LNGS scientifc commitee. LNGS-EXP 33/05 add 5/07.

[15] http://hepwww.rl.ac.uk/ukdmc/Radioactivity/uk.html.

[16] Leonard D.S. et al. Systematic study of trace radioactive impurities in candidate construction material for EX0-200. *Nuclear Instrument and Methods in Physics Research A*, 591:490–509, 2008.

[17] http://hepwww.rl.ac.uk/ukdmc/Radioactivity/hs.html.

[18] http://borex.princeton.edu/public-docs/theses/cadonati_phd_by_chapter/cadonati_phd_ chapter8.pdf.

[19] http://radiopurity.in2p3.fr/.

[20] Aprile E. et al. Material screening and selection for XENON100. *arXiv:1103.5831*, V1, 30 Mar 2011.

[21] Kobayashi K. et al. XMASS Experiment. *TeV Particle Astrophysics Conference*, 2010. Paris.

[22] Aprile E. et al. Design and performance of the XENON10 Dark Matter Experiment. *arXiv:1001.2834*, V1, 16 Jan 2010.

[23] NEXT radiopurity working group. NEXT radiopurity report and NEXT radiopurity data base http://gifna.unizar.es/radiopurity/main/login.php?next.

[24] F. J. Iguaz Gutiérrez. *Development of a time projection chamber prototype with micromegas technology for the search of the double beta decay of* ^{136}Xe. PhD thesis, Zaragoza, Universidad de Zaragoza, Zaragoza, Feb 2010. Presentado: 25/02/2010. http://zaguan.unizar.es/record/5731.

[25] H.T. Wong, D.A. Imel, V. Jrgens, M. Treichel, and J.-C. Vuilleumier. Event identification with a time projection chamber in a double beta decay experiment on 136xe. *Nuclear Instruments and Methods in Physics Research Section A: Accelerators, Spectrometers, Detectors and Associated Equipment*, 329(1-2):163 – 172, 1993.

[26] P.N.B. Neves, C.A.N. Conde, and L.M.N. Tvora. Drift field limitations to the energy resolution in time projection chambers for 136xe neutrinoless double beta decay search. *Nuclear Instruments and Methods in Physics Research Section A: Accelerators, Spectrometers, Detectors and Associated Equipment*, In Press, Accepted Manuscript:–, 2011.

[27] Tomás R. Rodríguez and Gabriel Martínez-Pinedo. Energy density functional study of nuclear matrix elements for neutrinoless $\beta\beta$ decay. *Phys. Rev. Lett.*, 105(25):252503, Dec 2010.

[28] J. Menndez, A. Poves, E. Caurier, and F. Nowacki. Disassembling the nuclear matrix elements of the neutrinoless [beta][beta] decay. *Nuclear Physics A*, 818(3-4):139 – 151, 2009.

[29] D. Decamp et al. ALEPH: A DETECTOR FOR ELECTRON - POSITRON ANNIHILATIONS AT LEP. *Nucl. Instrum. Meth.*, A294:121–178, 1990.

[30] S. Afanasev et al. The NA49 large acceptance hadron detector. *Nucl. Instrum. Meth.*, A430:210–244, 1999.

[31] V. Eckardt et al. Calibration of the STAR forward time projection chamber with krypton-83m. 2001.

[32] L. W. Kastens, S. B. Cahn, A. Manzur, and D. N. McKinsey. Calibration of a Liquid Xenon Detector with Kr-83m. *Phys. Rev.*, C80:045809, 2009.

[33] K. Ni et al. Preparation of Neutron-activated Xenon for Liquid Xenon Detector Calibration. *Nucl. Instrum. Meth.*, A582:569–574, 2007.

[34] NEXT vessel working group. NEXT vessel report.

[35] P. Abbon et al. The Micromegas detector of the CAST experiment. *New J. Phys.*, 9:170, 2007.

[36] S. Aune et al. New Micromegas detectors in the CAST experiment. *Nucl. Instrum. Meth.*, A604:15–19, 2009.

[37] J. Galan. Micromegas detectors in the CAST experiment. talk given at the Workshop on Micropattern Gas Detectors, 12-17 June 2009, Kolympari, Crete, Greece. http://candia.inp.demokritos.gr/mpgd2009/.

[38] K. Graham. Talk given at the 5th Symposium on TPCs for Low Energy Rare Event Detection, Paris, 14-17 December 2010.

[39] J.F.C.A Veloso, J.M.F.dos Santos, and C.A.N Conde. Performance characteristics of a gas proportional scintillation counter coupled to a microstrip gas chamber photosensor. *Nuclear Instruments and Methods in Physics Research Section A: Accelerators, Spectrometers, Detectors and Associated Equipment*, 422(1-3):273 – 277, 1999.

[40] D. Franco. Talk given at the 5th Symposium on TPCs for Low Energy Rare Event Detection, Paris, 14-17 December 2010.

[41] D. Nygren. Talk given at the 5th Symposium on TPCs for Low Energy Rare Event Detection, Paris, 14-17 December 2010.

[42] B.D. Ramsey and P.C. Agrawal. Xenon-based penning mixtures for proportional counters. *Nuclear Instruments and Methods in Physics Research Section A: Accelerators, Spectrometers, Detectors and Associated Equipment*, 278(2):576 – 582, 1989.

[43] D. Walker. Talk given at the 5th Symposium on TPCs for Low Energy Rare Event Detection, Paris, 14-17 December 2010.

[44] I. Giomataris. Talk given at the 5th Symposium on TPCs for Low Energy Rare Event Detection, Paris, 14-17 December 2010.

[45] C. M. B. Monteiro et al. Secondary Scintillation Yield in Pure Xenon. *JINST*, 2:P05001, 2007.

[46] L.C.C. Coelho, J.A.M. Lopes, D.S. Covita, A.S. Conceio, and J.M.F. dos Santos. Xenon gpsc high-pressure operation with large-area avalanche photodiode readout. *Nuclear Instruments and Methods in Physics Research Section A: Accelerators, Spectrometers, Detectors and Associated Equipment*, 575(3):444 – 448, 2007.

[47] J. A. M. Lopes, J. M. F. dos Santos, R. E. Morgado, and C. A. N. Conde. A xenon gas proportional scintillation counter with a uv-sensitive large-area avalanche photodiode. *IEEE TRANSACTIONS ON NUCLEAR SCIENCE*, 48(3), 2001.